Title
Isotope-Specific Detection and Assay: Engineering Solution with Directional Nuclear Resonance Fluorescence

Author
Semenov, Vladimir Alexandrovich

Publication Date
2014

Peer reviewed|Thesis/dissertation

Isotope-Specific Detection and Assay:
Engineering Solution with Directional Nuclear Resonance Fluorescence

by

Vladimir Alexandrovich Semenov

A dissertation submitted in partial satisfaction of the

requirements for the degree of

Doctor of Philosophy

in

Engineering–Nuclear Engineering

in the
Graduate Division

of the

University of California, Berkeley

Committee in charge:

Professor Edward Morse, chair
Professor Joonhong Ahn
Professor Eric Norman
Professor Stuart Bale

Spring, 2014

Abstract

Isotope-Specific Detection and Assay:

Engineering Solution around Directional Nuclear Resonance Fluorescence

by

Vladimir Alexandrovich Semenov

Doctor of Philosophy in Engineering–Nuclear Engineering

University of California, Berkeley

Professor Edward Morse

In this work we endeavor to engineer a new tool for isotope-specific assay and detection. We propose to utilize Nuclear Resonance Fluorescence (NRF) as the process that gives isotope-specific information about the object under investigation. Careful experimental and theoretical studies of angular dependencies of signal (NRF) and noise (other significant scattering channels) are presented. These studies motivate engineering design of detector array exploiting signal vs. noise discrepancies in angular distributions. User-defined materials of interest, detection / assay times and accuracy requirements inform the design yielding optimal performance.

I would like to dedicate this work to three people who made this work possible.

Dr. Christopher Ebbers – who mentored, encouraged and worked behind the scenes enabling and empowering this work.
Dr. Edward Morse – who gave me a shot at being a part of UC Berkeley graduate school, who encouraged, prodded, and finally insisted I get this done.
Elise Morris – I love you. Thank you for all your help and encouragement.

List of figures.

List of Tables.

Chapte 1: Introduction

This thesis addresses five challenges concerning nuclear materials, ranging from nuclear non-proliferation to cancer research. Meeting those challenges has directed the creation of a list of specific requirements. The solution must be **noninvasive, fast, nonactivating, accurate,** and **low dose to target and environment**. This work presents an approach that solves the challenges and satisfies the requirements. This thesis is the theoretical, experimental, and engineering study of this approach.

1.0 Definition of terms and acronyms

Nuclear materials is a collective term including all isotopes of Uranium (U) and Plutonium (Pu) and their decay products. All the elements and isotopes that can be encountered in nuclear fuel, that could be used in nuclear weapons, and are of concern in nuclear waste are collectively referred to as nuclear materials.

The material (isotope) of interest is an isotope of the element that needs to be found or studied. Pu239 in spent fuel rods, toxic isotopes in nuclear fuel waste, and telltale calcium in a suspicious tumor are all examples.

The object under investigation is an object that might or might not contain a material of interest. A spent fuel rod, a cargo container, and a sample of biological tissue are all examples of objects under investigation.

Detection involves deciding whether the object under investigation contains a material of interest. This is a yes or no process. The decision must be statistically significant and must be in accordance with user-defined requirements. These requirements are: false positive probability, false negative probability, maximum time of determination, and the threshold amount of isotope of interest.

Assay refers to the process of determining how much of the isotope of interest is in the object under investigation. Assay results in a number with error bars. User-defined requirements here are accuracy (error bars on the amount of material), scan time, and the certainty of the measurement.

Burnup fraction is a fraction of fuel atoms that underwent fission.

Dose (radiation dose) is a measure of the total amount of ionizing radiation absorbed by materials.

Activation (neutron activation) is the process in which neutrons induce radioactivity in materials.

Nuclear resonance fluorescence (NRF) is the resonant scattering of a photon by a nucleus. The photon's energy must exactly match the energy difference between two nuclear energy levels. Energy levels are isotope specific, so this effect enables of isotope specific spectroscopy.

Compton Scattering refers to the interaction between a photon and an electron. This is an inelastic collision—the photon loses energy. There is a significant angular dependence of the process due to the linear polarization of interacting photons. This is a dominant mode of photon-matter interaction at the energies studied.

INMM: Institute of Nuclear Materials Management, the organization for promoting R&D in the fields of waste management, non-proliferation, and security. The INMM is the platform to formulate the challenges addressed in the thesis.

LLNL: Lawrence Livermore National Laboratory.

SLAC: Stanford Linear Accelerator.

T-REX: Thomson Radiated Extreme X-ray.

HIγS at TUNL: High-Intensity Gamma Source at Triangle Universities National Lab. Duke University is the physical location of the gamma-ray source.

In this work, the terms "gamma-ray," "gamma," and "photon" are used interchangeably. The author is aware of the strict definition of gamma-ray as only a photon that has been produced by a nuclear reaction. Nevertheless, this thesis uses those terms to denote any quantum of electromagnetic radiation that has energy in excess of 100 keV.

1.1 Overview

This thesis discusses the engineering design of a device for isotope-specific detection and assay of nuclear materials. Chapter 1 explains the approach chosen and provides an overview of the state of corresponding technologies. The theory chapter, Chapter 2, overviews gamma-ray/matter interaction channels to come up with a comprehensive theoretical picture of the physics involved. The experimental chapter, Chapter 3, describes the experiment that is used to test the theoretical prediction to be fed into the engineering design. The engineering design chapter, Chapter 4, describes the detector system that uses directional nuclear resonance fluorescence as an information carrier about the material of interest. Chapter 4 also discusses decision metrics

and information processing approaches that optimize detection/assay times. The thesis concludes with Chapter 5, the discussion of possible hardware developments and their impact on the field.

In the first chapter, we present several applications for isotope-specific detection and the assay of nuclear materials. Each application formulates a list of requirements to be met. Those requirements are combined into a list. Directional NRF meets the list of requirements. The next section gives an overview of the gamma-ray sources capable of exciting NRF. Narrow-band gamma-rays, produced by Compton Scattering of polarized light, can meet the requirements of the applications presented. This chapter culminates in a description of two sources that successively studied NRF: T-REX and HIγS. An overview of an experiment at HIγS is provided as context for the theory discussion.

1.2 Applications of isotope-specific detection and assay: List of requirements

The numerous applications for isotope-specific detection and assay require additional experimental, theoretical, and engineering effort. The following is the discussion of several opportunities in the areas of nuclear materials management, nonproliferation/homeland security, and medicine. Each example concludes with a list of requirements for the solution (in bold). This drives the list of requirements for the detection system needed in order to meet the challenges discussed.

Nuclear power plants face the continual challenge of managing nuclear fuel and nuclear waste. Decisions such as where to insert a particular rod in the fuel assembly and how long to keep the rod in each position are motivated by the fraction of the original U235 inventory left in the rod, known as the *burnup fraction*. In the reactor core, nuclear fuel is exposed to a neutron flux, causing fission to occur. Fission depletes the U235 inventory in the fuel rod and creates decay products until the end of the decay chain. However, it is difficult to measure the spatial profile of the neutron flux inside the working reactor—a problem further compounded by the inability to accurately estimate the original isotopic content in the particular rods. Due to these uncertainties, current burnup fraction models require users to estimate many parameters. Typically, a fuel rod is deemed spent after three years in the reactor. While this estimate might be appropriate for certain rods, it might be too low for other rods. An accurate burnup estimate would extend the fuel rod work time, saving both money and time spent replacing the rod.

Current techniques to determine the isotopic composition of spent nuclear fuel rods are invasive, expensive, and risky. The rods must be de-clad, and the elements must be chemically separated for further isotopic analysis. Although this approach provides an isotope inventory on a single spent fuel rod, it is too unwieldy to be universally applicable. For fuel rod management decisions there is a need for a noninvasive, fast, and accurate way to determine the isotopic content of the fuel rod both before and after irradiation. This will increase the average life of the fuel rods.

Furthermore, the neutron flux profiles in the reactors could be inferred accurately from the "before" and "after" pictures of the isotope inventory in the fuel rods. Let's summarize the requirements for the application (each application will have a summary of requirements in bold).

Requirements for nuclear fuel management: The assay must be **non-invasive, fast, accurate**, and **able to detect various isotopes**.

An additional challenge in nuclear power generation as it pertains to the fuel cycle is nonproliferation. Management of completely spent nuclear fuel rods requires maintaining an accurate account of Pu239 inventories. This material, which can be used to make a bomb, is created in the reactor and can be chemically separated with relative ease (i.e., there is no need for centrifugation). The INMM is most concerned about the "substitution" scenarios where spent Pu-laden fuel rods are replaced with fresh fuel rods, allowing miscreants to divert Pu239 for nefarious purposes. A quick and reliable way to determine the Pu239 content of every rod would enable tracking of the spent fuel rods, minimizing potential theft of the rods. Once again, requirements for this challenge get their own paragraph.

Requirements for spent nuclear fuel accounting and safeguarding: The assay must be **fast and accurate.**

Nonproliferation concerns motivate a "nuclear carwash" concept for scanning cargo containers in ports and airports. A national security goal is to better guard against potential "dirty bomb" scenarios. Strategically placed conventional explosives used to disperse nuclear material over a large area would be extremely disruptive to the economy of the United States. This increases the need for detection of nuclear material inside a cargo container. Expediency in managing cargo containers requires a relatively low dose, a low rate of false positives, and fast scanning.

Requirements for national security non-proliferation: The detection/assay must be **noninvasive, fast, accurate** (low rate of false negatives**), nonactivating,** and **must limit the dose to the environment**.

The proposed approach has various medical applications which have strict requirements on maximum radiation dose. Two examples are isotope tracking in a medical patient, and exact isotope assaying of a patient's tissues. Several types of cancerous tissues are thought to contain higher levels of certain elements compared to healthy tissue. An exact measurement of the amount of calcium, for example, could be used as a detection tool for early stages of cancer. Such methods of assaying yield life-saving information. Additionally, a lower-dose detection approach would greatly improve the tracking of specific isotope markers as they travel through a patient's body.

Requirements for medical applications: An approach that is **noninvasive and** nonactivating**, and** that **limits the dose** to both the environment and the patient.

Taking all of the above requirement scenarios into account, the detection/assay must be **noninvasive, fast, nonactivating, accurate,** and **low dose to target and environment**. It is therefore crucial to evaluate potential approaches to the detection/assay of radioactive materials based on these requirements.

1.3 Selection of an approach capable of satisfying the requirements

We endeavor to check all possible approaches to the detection/assay against the list of requirements from section 1.1. Essentially, this will eliminate some approaches and impose conditions on others. Finally, the best way to tackle the problems will emerge.

There are three ways to analyze a material for isotope composition: chemically, passively, and actively. The chemical method of detection involves a partition of the elements in the material via chemical manipulations. The passive method of detection analyzes the signal out of the undisturbed sample, inferring the composition from various reaction products. Finally, one can induce a reaction in the material. Detecting tell-tale signs of the reaction thus induce constitutes active detection method.

The previously identified noninvasive requirement precludes the chemical approach.

The passive method of interrogation calls for the detection of certain telltale signs indicating that an isotope of interest is present. If an isotope of interest is involved in a nuclear reaction with unambiguous particle yield (specific neutron or gamma-ray energy, where multiple particles are created with certain energies), then detection of these products is indicative of the isotope of interest. All passive approaches require a nuclear reaction to occur. In the isotopes of interest for the nuclear community, the spontaneous processes utilized are not very fast. Additionally, it is even slower to accumulate statistics using multiple particle coincident detections, due to the low probability of simultaneous particle detection. Due to these limitations, passive approaches are unacceptably slow.

Active methods cause something to occur in the isotope of interest. The presence of this isotope affects how the object will react to the probing beam. The investigating beam intensity determines the occurrence rate, allowing such methods to potentially **be as fast as necessary.**

Active methods of investigation differ from passive methods in that they cause the isotope of interest to react. It is possible to induce fission in the isotope of interest. One of the previously identified requirements is that the assay should be **nonactivating**. Nonactivating processes are

either scattering or fluorescence. Charged particle scattering is not isotope specific, as it is dominated by Coulomb scattering. This means that the atomic charge number Z of the isotope determines the scattering of the charged particle. Gamma-ray fluorescence is the only process that minimizes the chance of activation, because neutron scattering risks activation of the object under investigation.

Spectroscopic approaches in general are divided according to whether the analyzed spectra are transmitted or reflected. Several targets of interest are radioactive (e.g., nuclear fuel rods), causing a large background signal, which lengthens the time it takes to analyze a spectrum beyond a practical limit. Quiter et al. (1) present a comprehensive analysis of how detection times are affected by the background. Reflection spectroscopy does not meet the need for the detection/assay to **be fast**. Transmission spectroscopy is thus chosen.

To minimize the dose to the detectors from the object under investigation, a witness foil behind a detector wall is necessary. This allows for there to be no direct line of sight between the object under investigation and the detector. Gamma-rays scattered by the witness foil onto the detector are analyzed for information about the transmitted spectrum of interest. It is possible to minimize the background from radioactive objects under investigation (Figure 1.1). **Low dose to target and environment** is thus achieved.

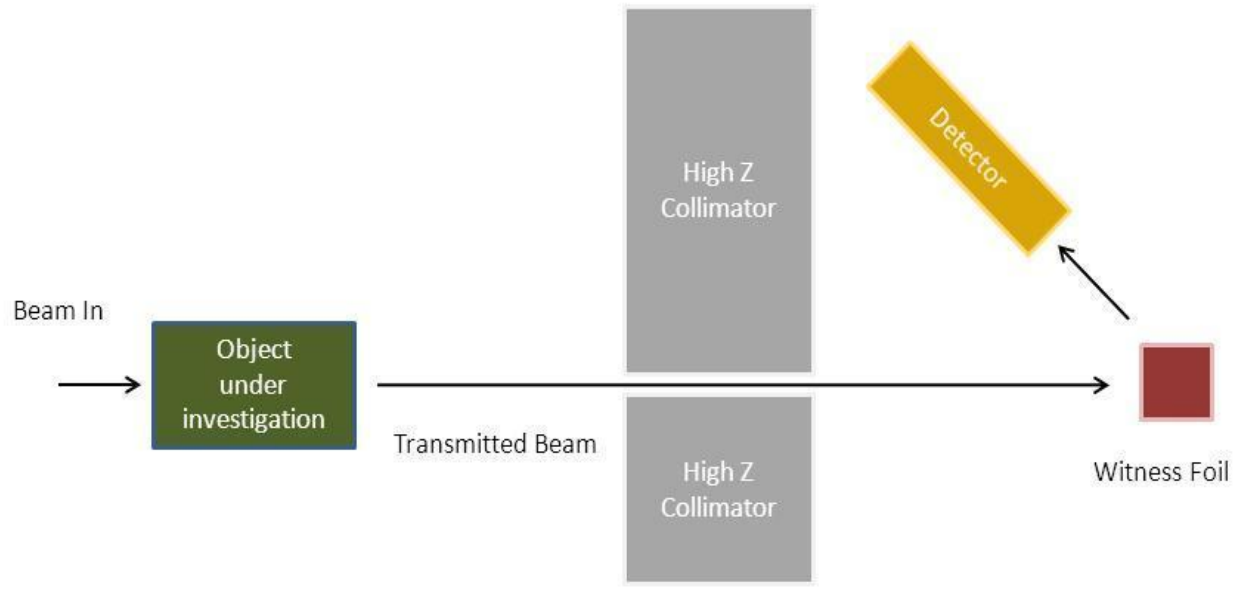

Figure 1.1. Transmission spectroscopy setup with a witness foil: no line-of-sight between object and detector.

It is necessary to select a process for active interrogation that is sensitive to different isotopes. Each isotope has a unique energy level structure. The transitions between nuclear energy levels

constitute an unambiguous signature. NRF is a process of absorption and re-emittance of a gamma-ray by the nucleus of an isotope (Figure 1.2).

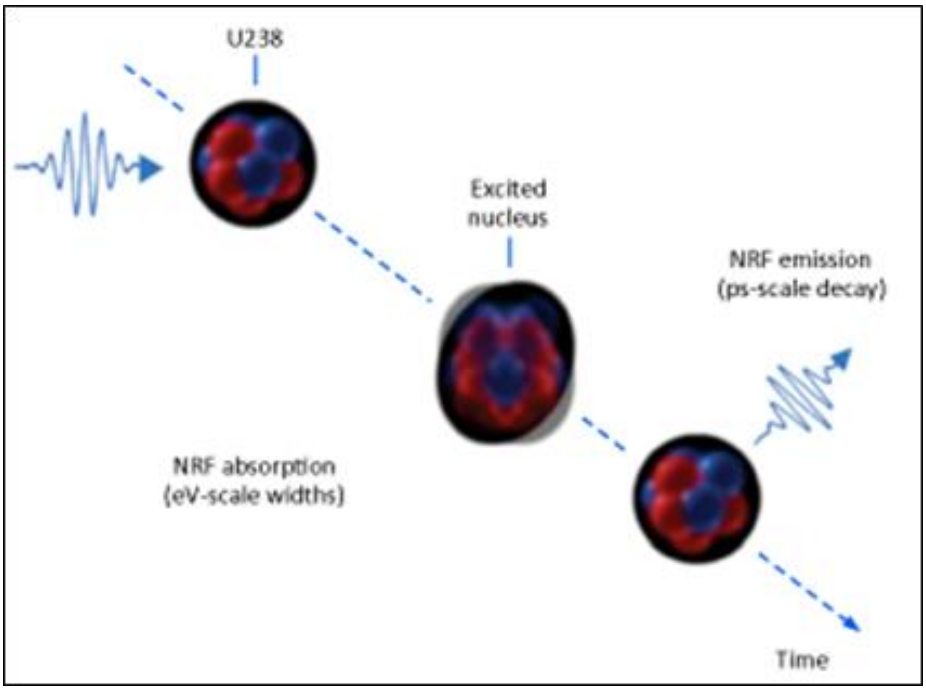

Figure 1.2. Nuclear resonance fluorescence as absorption and emission.

The nucleus absorbs gamma-rays of energy corresponding to the energy level difference. Due to this phenomenon, NRF is suitable for accurate detection and assay. The typical width between NRF lines is on the order of an electron Volt (eV) (Doppler-broadened), minimizing potential confusion between different resonances. Thus we get **accurate** assay/detection.

An additional method of determining accuracy is to compare the cross-sections of signal-generating processes to those of noise-generating processes. Once again, NRF is a strong candidate with respect to this method. Typical lines have tens of eV-barns integrated cross-sections, and certain lines have up to thousands of eV-barns. These high cross-sections combined with the narrowness of NRF lines, means that fluorescence is the dominant process at the energy of occurrence. Even binning the spectra in 2-3 keV bins does not weaken the NRF versus non-NRF count discrepancy. During the experiment at HIγS (described in Chapter 3), bins that include NRF energies accumulated statistically higher counts very fast. The high integrated cross-section combined with the narrow bandwidth of the effect potentiates the design of a **fast** and **accurate** detection and assay.

In order to use NRF, the interrogating beam must contain many NRF-capable photons. The number of photons determines the speed and accuracy of detection or assay. The total number of

photons in the beam determines the optimal dose to the object under investigation and to the environment. To satisfy the last identified requirement—**Low dose to target and environment**—the beam must be low in flux. Quasi-monoenergetic gamma-ray sources satisfy both the high number of NRF-capable photons requirement and the low total flux requirement and are applicable to safeguards, as discussed by Johnson et al. (2).

Transmission-based gamma-ray spectroscopy is a promising technique to develop assays that are noninvasive, fast, and nonactivating. To minimize the dose to the target and the environment while maintaining a high level of speed and accuracy, NRF using a quasi-monoenergetic source is another promising alternative.

1.4 Gamma-ray sources capable of exciting NRF

Nuclear resonance fluorescence has been observed using a number of gamma-ray sources. In this section, we overview and compare three possible ways to produce gamma-rays capable of exciting detectable amounts of nuclear fluorescence. Bremsstrahlung sources have high potential flux. Those sources are broadband sources—all energies up to generating energy are presented in the spectrum. Thus, those sources are inherently very noisy. A second approach (reference 3) uses isotopes of interest to produce a probing beam of gamma-rays. Finally, Compton-based gamma-ray sources are capable of satisfying all the requirements outlined in the previous section.

Bremsstrahlung is electromagnetic radiation produced by deceleration of the charged particle. Jackson (4) discusses the relativistic formula for power radiated:

$$P = \frac{q^2\gamma^6}{6\pi\varepsilon_o c}\left(\left(\frac{d\underline{\beta}}{dt}\right)^2 - \left(\underline{\beta} \times \frac{d\underline{\beta}}{dt}\right)^2\right)$$
$$\gamma = \frac{E}{mc} \qquad (1.1)$$

Power radiated depends on the 4th or 6th power of gamma, depending on the direction of the radiation. The radiating particle needs to be light for high power yield, because gamma is inversely proportional to it. Thus most practical applications use electrons as the radiating particle. It is easy to increase the output of bremsstrahlung sources by simply increasing the charge accelerated in order to increase the number of radiating electrons. These sources have been used for detection of NRF lines and measurement of their energies (once again, 3).

The drawback of the bremsstrahlung approach is that it is broadband—all energies up to the energy of the radiation generating beam are present in the spectrum. Therefore, the ratio of NRF-capable photons to the total flux is virtually zero. Previous studies were concerned only with the detection of nuclear resonances and so were not concerned by this limitation; in experimental

science at its purest, time of detection is not a driving engineering design concern. For the proposed applications' requirements of speed and accuracy, a high signal-to-noise ratio is crucial, so the spectral width of the source is paramount. Unfiltered, unmodified bremsstrahlung radiation is not a feasible method to use to satisfy the requirements.

Using the reasoning "the narrower the spectrum, the better," the gamma-ray beam may be thought of as the optimal width, i.e., the energy width of the desired resonance. If every photon in the probing beam is capable of exciting the signature transition, the resulting signal-to-noise ratio is the biggest possible. The approach used by Metzger (3) endeavors to achieve this. Consider only NRF for a moment. The primary source of radiation impinges on the disk that is made out of the isotope of interest. This excites NRF in the disk. Re-emitted photons constitute the probing beam. During the absorption and reemission of the photon that constitutes fluorescence, conservation of momentum requires the nucleus to acquire recoil energy. Thus, re-emitted photons are a few tens of eVs off-resonance if the disk is stationary. If the disk is rotating at a correct speed, it is possible to compensate for the recoil to construct a perfect probing beam where the energy spectrum of photons exactly matches the resonance energy spectrum.

The reality is somewhat more complicated: In the disk we can have both elastic and inelastic non-NRF scattering. The experimental setup described by Metzger (3) increases the fraction of gammas capable of NRF very effectively, but a number of off-resonance photons still remain in the probing beam. There is no clear engineering path to increase the beam quality after the rotating disk.

This approach works ideally when the isotope of interest is nonradioactive. In this case, the beam-forming disk does not add anything to the beam; it simply emits NRF gammas, for the most part. Most of the proposed applications seek to detect and assay radioactive isotopes. This implicates that the beam-creating disk would be radioactive, adding further shielding challenges. Furthermore, activity in the disk would amplify noise because nuclear reactions in the disk produce unwanted radiation. Finally, nuclear reactions' products pose a serious risk of unwanted activation.

In addition, using a set of disks for multi-isotope assay adds engineering complexity because the velocities of rotation in each case must be fine-tuned, because recoil is isotope mass dependent and the width of the resonance is very small.

Compton scattering is the process chosen for creation of the probing beam for the proposed applications (1). Geometry of the interaction is presented in Fig.1.3.

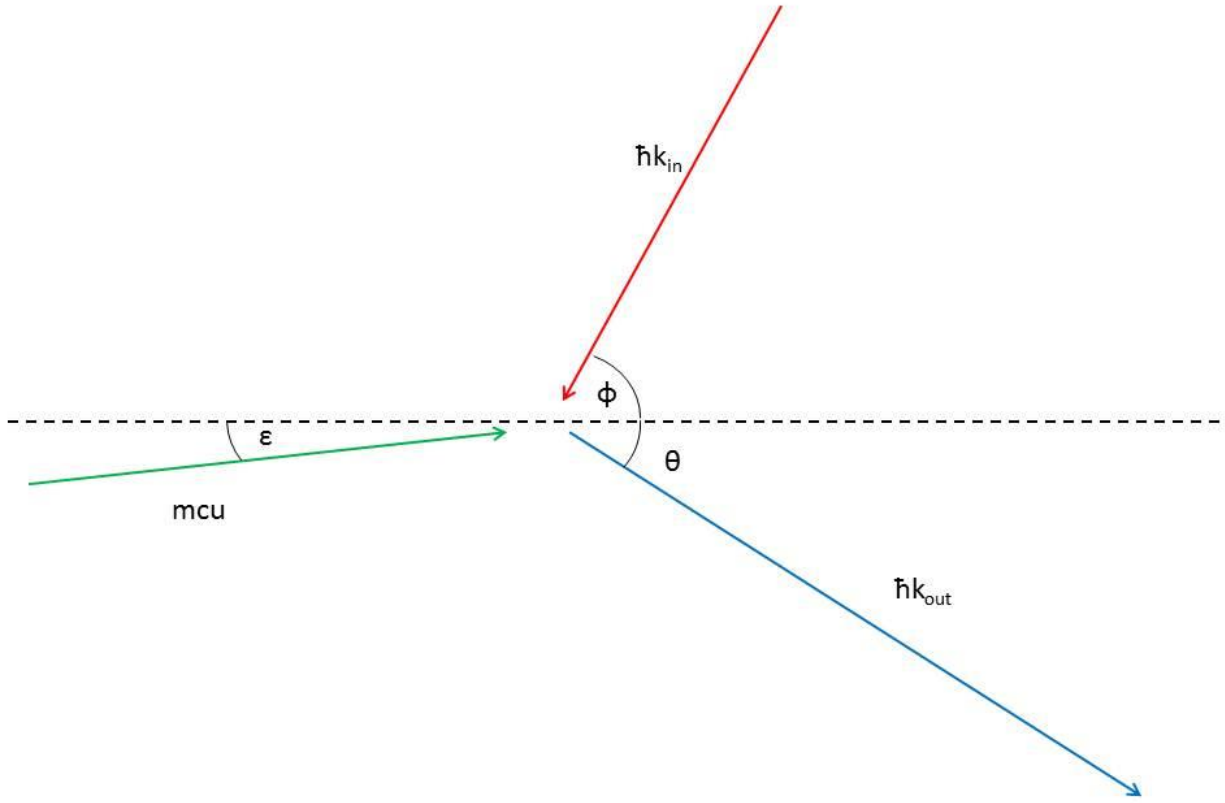

Figure 1.3. Compton scattering geometry. Photon's momentum increases from $\hbar k_{in}$ to $\hbar k_{out}$. All angles are measured with respect to the electron beam path. Electron momentum is represented to have "u" to be unitless. This can be achieved by defining "u" as a ratio the momentum to "mc".

In this phenomenon, a carefully prepared electron bunch interacts with a pulse of photons. The photons shift up in energy into gamma-ray range. This creates a beam whose energy can be controlled by varying the electron energy. Bandwidth is determined by properties of the interacting electron bunch and laser pulse (reference 5 presents the theoretical computation behind formula 1.2).

$$k_{out} = k_{in} \frac{\gamma - \mathrm{u}\cos(\varepsilon + \phi)}{\gamma - \mathrm{u}\cos(\varepsilon) + (1+\cos(\phi))\{\frac{A^2}{2(\gamma - \mathrm{u}\cos(\varepsilon+\phi))} + \lambda k_{in}\}} \quad (1.2)$$

Where A is related to the intensity of the electromagnetic field and λ is Compton wavelength. Variation analysis yields how bandwidth of the outgoing gamma-ray beam ($\frac{\Delta k_{out}}{k_{out}}$) relates to variations in all other parameters (those parameters are traced to the measurable quantities)

Source aperture: $\frac{\Delta k_{out}}{k_{out}} \approx -\gamma^2 \ \Delta\theta^2$

Laser bandwidth: $\frac{\Delta k_{out}}{k_{out}} \approx \frac{\Delta k_{in}}{k_{in}}$

Laser focal spot: $\frac{\Delta k_{out}}{k_{out}} \approx -\frac{1}{4} \ \Delta\phi^2$

Electron energy spread: $\frac{\Delta k_{out}}{k_{out}} \approx \frac{\Delta\gamma}{\gamma}$

Electron beam emittance: $\frac{\Delta k_{out}}{k_{out}} \approx -\gamma^2 \ \Delta\varepsilon^2$

Nonlinear radiation pressure: $\frac{\Delta k_{out}}{k_{out}} \approx -\frac{\Delta A^2}{1+A^2}$ (1.3)

Thus, there is a clear engineering path to achieve better probing beams in flux and bandwidth. Source aperture, electron energy spread, and beam emittance are limiting parameters in current state-of-the art machines. The other three do not appreciably spread out the bandwidth.

Furthermore, this is the only approach that creates highly polarized gammas; polarization of the beam is determined by polarizations of interacting particles. Laser light is polarized, and electrons are controlled by accelerator technology. The Compton-based source would give us a tunable, narrow-band, high-flux, quasi-monochromatic, quasi-collimated, polarized gamma-ray beam, which is ideal for the applications discussed above.

1.5 Overview of hardware for polarized gamma-ray source

Compton scattering requires energetic electrons to upshift the photons in the laser pulse. A laser pulse is required to create an electron bunch at the photocathode; an accelerator then accelerates the electron bunch, and lastly an ultra-short pulse of laser light interacts with the electrons. Each of these three subsystems poses its own engineering challenges, and there are historically different methods of overcoming these challenges.

Consider how all these technologies can be brought together to a produce a gamma-ray source:

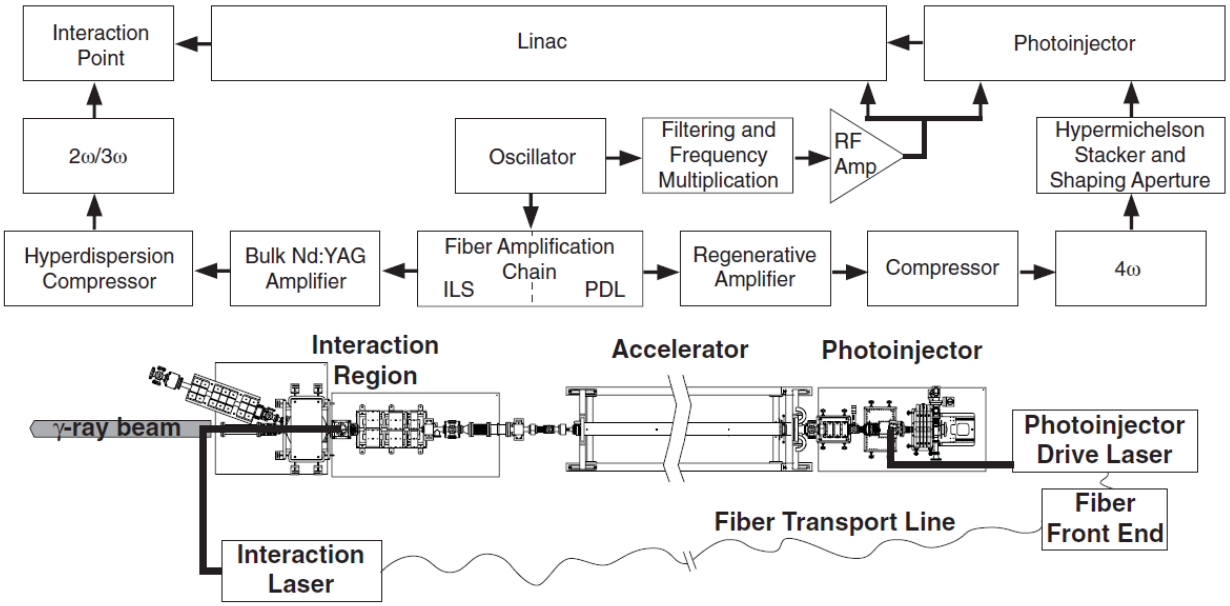

Figure 1.4. Schematic of the gamma-ray source, reproduced from (6): "Top: A block diagram of the T-REX system, showing all the subcomponents described in detail in the text. Bottom: A Schematic of the integrated system".

The seed oscillator's output is divided into two paths. One path traverses the photo drive laser (PDL) system and impacts the photocathode. Electrons produced in this manner are accelerated in the linac for delivery at the interaction point. The second path shapes the seed into a laser pulse, which is then scattered into electrons at the intersection point.

The PDL system is a fiber-based laser. A pulse is stretched, amplified, and compressed to produce a laser pulse with parameters suitable for proper electron bunch production. The compressed laser pulse is, in an ideal case, Gaussian in space and time. It is thought that the electron bunch profile should be sharply circular in space and square in time. An ideal shape for the electron bunch is hypothesized to be a right cylinder with an axis of rotation parallel to the beam path axis, which can be approximated by Gaussian beams stacked on top of each other. The hyper-Michelson stacker, as described by Gibson et al. (6), creates the final shape for the PDL laser output.

An electron gun receives the PDL output and outputs an electron bunch. In the experiment performed by Gibson (6), the electron bunch was demonstrated to be of the desired spatial and temporal distribution.

The laser pulse to undergo Compton scattering can be created through different laser systems. Previous sources have used various laser systems: Ti:sapphire (7), fiber (8), and a free electron (9). The last-mentioned system was used for experimental confirmation of the theoretical

formulas discussed in Chapter 2. The free electron laser wiggles the electrons in the lasing cavity to create light. This light meets the next electron bunch to generate a gamma-ray. This collision is automatic in time and space, because both the electrons and the photons travel along the same beam path.

In non-FEL based systems, timing the arrivals of the electrons and the laser pulse is challenging. These events occur on a nanosecond timescale, making simultaneous arrival difficult to orchestrate. By using the same seed for both systems, this challenge can be eliminated. Starting from the same seed, the signal is split down two paths: the photodiode, and the interaction region. Each path prepares the laser pulse specifically for its subsequent task—either knocking out electrons from the photocathode via a photoelectric effect, or interaction with the accelerated electron bunch after the x-band linac. Each path has a fixed time of flight; therefore, electron-photon synchronization at the interaction point is most concerned with introducing an appropriate delay to one path for the exact arrival time of the two paths to match.

1.6 Two gamma-ray sources used in NRF experiments: T-REX and HIγS

Classical radiography detects density variations. Absorption of x-rays is determined by the density of the material scanned. Higher-density compounds appear dark in the image because denser beam paths scatter more photons. The T-REX experiment was the first to demonstrate inverse density radiography by detecting the less-dense material lithium behind denser lead. Compton scattering occurred between s-band accelerated electrons and titanium-sapphire amplified laser pulses. This interaction created gamma-ray beams of low divergence (milliradians), ~10% spectral width, and 2 NRF-capable gammas per second flux. A single-photon counting technique with appropriate binning enabled unambiguous detection of the lithium behind the lead.

The high-intensity γ source (HIγS) is an installation of the Triangle University National Laboratory (TUNL) at Duke University in North Carolina. This source collides FEL-produced photons with electron bunches from the linac upstream. Every electron bunch creates a number of green photons in the FEL area and then interacts with previously created photons to produce gamma-rays. Thus, the repetition rate of the source is determined by the repetition rate of the photocathode upstream (MHZ). Laser light and electron beam qualities using this technique are significantly better than with T-REX, explaining the narrower bandwidth. The stability of this source enables systematic studies of nuclear resonances.

1.7 HIγS and Pb206 detection/assay

Lead-206 has an exceptionally high NRF cross-section, which was the motivating factor to use it in the experiment discussed in this thesis. One of the goals was to study the angular distribution

of NRF and non-NRF scattering, which was made possible by detectors using several azimuthal and polar angles during the runs. Furthermore, all the runs were performed twice: once with an object upstream, and once without an object upstream. This object (a lead brick) was a stand-in for the object under investigation. Lead-206 in the brick represented the nuclear material being sought during the scans. Other isotopes in the brick represented isotopes and elements that are of no interest (e.g., healthy tissue in medical applications, or a container of nonthreatening cargo in transport applications).

The witness foil was a lead-206 disc (90.5%) that backscattered the gamma-ray beam onto three detectors at various positions. First, the foil was tested in-plane and out-of-plane of the polarization of the incoming beam. Second, all detectors were positioned to catch backscattering gammas at an angle to minimize noise from Compton scattering; angles above 100 degrees were found to be acceptable. Geometry dictated the maximum polar angle to be 150. At angles greater than 150, the detector shielding clipped the beam. NRF polar anisotropies contrast scattering at 180 vs. 90 degrees. Therefore, the polar angles were chosen to be as close to 180 and 90 as possible (Figure 1.5).

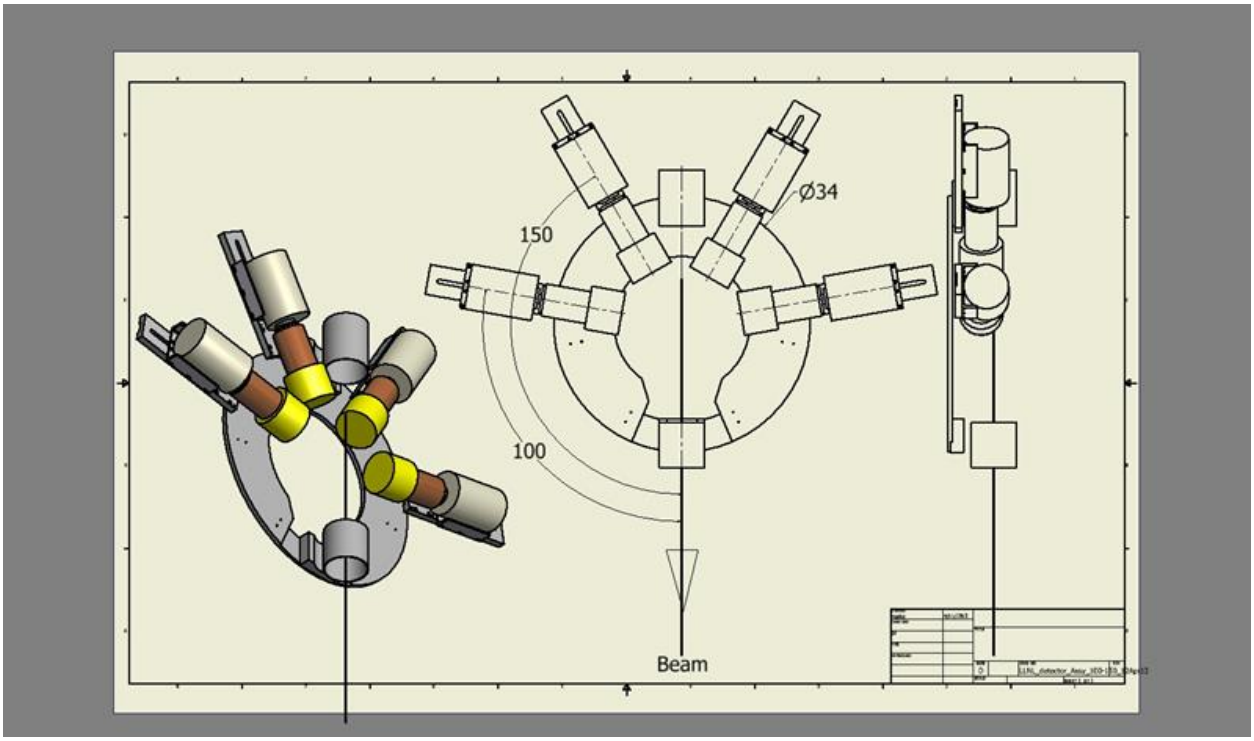

Figure 1.5. Detector array to be fixed at φ= 0 or 90 for the runs.

The experimental data includes detector outputs at different angles, with the brick in and out of the beam. Hour-long experimental fractions were integrated to provide data files to be analyzed. Background and calibration runs with various radioactive isotopes were also measured.

High-purity germanium (HPGe) detectors were utilized for data collection. Canberra's Genie and open source CODA software were used to record and histogram the data. Post-analysis of data was performed to correct for detector dead times, incomplete charge accumulations, and other detector-introduced distortions. The adjusted data is used to check the theoretical models from Chapter 2. This motivates the engineering design discussed in Chapter 4.

1.8 Conclusion

This chapter provided an overview of several challenges to the nuclear engineering community concerning the detection and assay of nuclear materials. The combined requirement list for techniques includes **noninvasive; fast; nonactivating; accurate; and low dose to target and environment**. Directional nuclear resonance fluorescence, an active interrogation technique, was identified as the engineering approach that satisfies the listed requirements. In this method, a transmitted beam impinges on the witness foil and then the angular spectrum of scattered light can be analyzed for detection or assay.

Chapter 2: Theory of polarized gamma-ray scattering

2.1 Assumptions

It is important to consider the assumptions made before any theoretical discussion can take place. In the parameter space of the experiments proposed, it is assumed that scattering events are not common. Additionally, the megavolts photon beams used are very penetrating. These assumptions allow analytical formulas to disregard multiple scattering events of a single photon.

Admittedly, it is necessary to include all possible scenarios for a photon's flight, however improbable they might be, for a mathematically exact analytical solution. Monte Carlo simulation of the experience takes all such scenarios into account. For the proposed engineering design, it is important to design a theoretical description that is accurate yet practical enough to use. In some cases, the description will account for the multiple interactions that a single photon can have but will ignore it in improbable scenarios.

When considering absorption processes—what occurs to the beam as it passes through the object under investigation—the air, the shielding, and the detecting medium will be treated with integrated cross sections from the reference available? Multi-scattering events are deemed improbable at these interfaces and can be disregarded. Scattering processes that occur in the witness foil are at the core of this work; therefore, multi-interaction scenarios in the foil are included in the consideration. Furthermore, the physics dictating interactions at the witness foil include directionality in the cross sections, because we can count only the photons that get scattered directly into the detector. Thus we use differential cross sections that take photon polarization into account.

The beam used is assumed to be a Gaussian beam, centered at the energy of the resonance. The beam's intensity and spectrum are considered constant throughout the experimental run. Lastly, the beam is considered to be 100% linearly polarized. Table 2.1 shows the exact parameters of the beam (taken from ref. 10).

$$\Phi(\mathrm{E}) = \Phi_0 * \frac{1}{\sqrt{\pi}*\delta} \mathrm{e}^{-((\mathrm{E}-\mathrm{E}_0)/\delta)^2} \tag{2.1}$$

Variable	Value	Description
Φ_0	10^8 photons/shot	total number of photons
δ	$.1$ MeV	
E_0	5.9 MeV	center of the beam

Table 2.1. Beam parameters.

The materials modeled are considered to be uniform in density with no voids. Surfaces are assumed to be ideally flat, and volumes are approximated to an ideal representation of their shapes (either cylinders or rectangular parallelepipeds).

The shielding configuration is considered to be completely effective, and therefore we do not need to account for transmission of the beam, although it is included in the models. The detectors are maintained at a constant temperature, geometry, and shielding during the runs; thus their response is assumed to be consistent for each detector. Backgrounds in the experimental chamber are measured and are considered consistent throughout the experiment modeled. Temperature, pressure, and humidity are recorded as constants in the equation.

2.2 General scattering formula

Probability of the scattering is directly proportional to the number of incident photons and the number of atoms exposed to the beam. The coefficient of proportionality in this relationship is called cross section of the scattering. This motivates the general formula for scattering probability:

$$\frac{dN}{dx} = -N(x)\sigma n$$
$$N(x) = N(0)e^{-\sigma n x} \qquad (2.2)$$

Where **N(x)** represents the number of gammas as a function of distance traveled, **n** is the density of the scatterer, and **σ** is the cross section of the interaction between gamma and scatterer. If multiple scatterers are present, we can rewrite the equation in terms of the i-th constituent:

$$dN = \Sigma dN_i$$
$$\frac{dN}{dx} = \Sigma \frac{dN_i}{dx} = -N(x)\,\Sigma\sigma_i n_i = -N(x)\mu$$
$$\mu = \Sigma\sigma_i n_i$$
$$\frac{N(x)}{N(0)} = N(0)e^{-\mu x} \qquad (2.3)$$

Where $1/\mu$ represents 1/e*(length of propagation), i.e., how far the beam needs to travel to drop in flux by a factor of natural log base. Formula (2.3) holds for scattering processes where the scattered photon disappears from consideration.

Because the beam is not monoenergetic, we need to take into account the energy dependence of the processes considered:

$$\frac{dN(E)}{dx} = -N(E,x)\sigma(E)n$$
$$\mu(E) = \Sigma\sigma_i(E)n_i$$
$$\frac{N(E,x)}{N(E,0)} = e^{-\mu(E)\,x} \qquad (2.4)$$

2.3 Formal description of nuclear resonance fluorescence

In the nucleus rest frame, resonant absorption is described by the Breit-Wigner formula. Krane defines the cross section as (combining 10.29 and 10.30 from ref. 11):

$$\sigma = \frac{2\pi}{k^2} * \frac{(2l_{exited}+1)}{(2l_{ground}+1)} * \frac{(\Gamma/2)^2}{(E-E_R)^2+(\Gamma/2)^2} \qquad (2.5)$$

Where k and E are the wave-vector and the energy of the photon undergoing resonant scattering respectively, and Γ and E_R are the width and the energy of the resonance respectively.

The excitation times before the gamma-ray is re-emitted are very short; thus, the natural width of the resonance is very narrow (uncertainty principle considerations limit it in at the micro-eV levels). Detecting such a narrow resonance is a challenging task. To complicate matters, the cross-section of the resonance is relatively large, causing the gammas within the narrow bandwidth to be scattered. The number of gammas in the micro-eV width would be prohibitively small to detect. Fortunately, there is an effect that broadens the resonance.

Formula (2.5) is in a frame of reference where the nucleus is stationary. In order to shift perspective to the frame of reference of the lab, it is necessary to take into account the thermal

motion of the nucleus. The Doppler Effect formula allows us to determine the frequency of photons emitted from the emitters' velocity. Ratio of the thermal velocity to the speed of light gives one energy spread due to thermal fluctuations. Statistical considerations set the Doppler broadening width to be ratio of thermal velocity to the speed of light. A practical calculation for the Lead 206 yields 3eV as the width of the resonance.

The width, δ, is significantly larger than the intrinsic width of the resonance, resulting in a convolution that is Gaussian around the resonance energy with the Doppler broadening width:

$$\sigma_{NRF}(E) = \sigma_0 * \frac{1}{\sqrt{\pi}\delta_{NRF}} e^{-((E-E_0)/\delta)^2} \quad (2.6)$$

$\sigma_0 = 2000\ \text{eV} - \text{barns}$ (integrated cross section of the resonance)

It is interesting to note the fact that Doppler broadening does not change the integrated cross section—it only broadens the width of the resonance. This is due to the fact that absorption depends only on the photon's energy. Broadening merely changes the shape of the absorption cross section, allowing more photons to participate. The fraction of incident photons scattered is identical with and without Doppler broadening. This relationship is mathematically captured by the following formula:

$$\sigma_0 = \int_0^\infty \sigma_{NRF}(E)dE \quad (2.7)$$

In this work, we endeavor to represent Gaussians with the normalization constant factored out in front as a first term in the product. Integrating (2.6) over all energies yields (2.7). Presented results are usually integrated over all energies, so the representation gives a quick visual way to assess the results.

The cross section discussed up until this point is for NRF absorption. After it is absorbed, the photon is re-emitted in a certain direction. We arrange the polar coordinate system to denote the directions with two angles: (θ, φ).

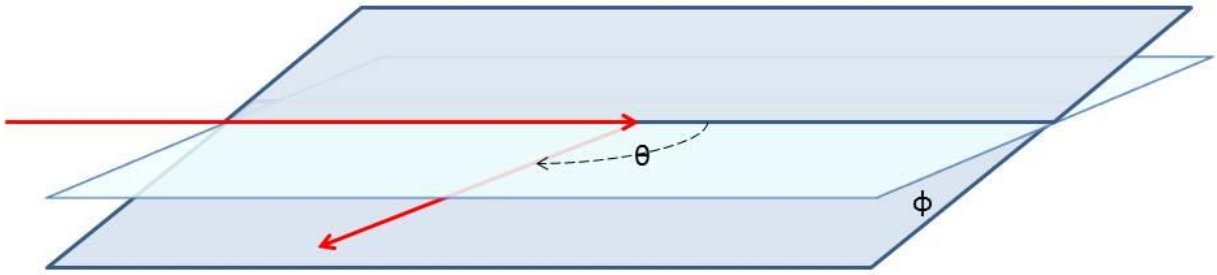

Figure 2.1. Polar coordinate system. Scattering angle denoted as θ, angle between horizontal plane and the plane of scattering denoted as φ.

The angular distribution of scattered radiation depends on the angular momentum of the resonant nucleus. Absorption of gammas must conserve angular momentum; therefore each photon can change the nucleus's angular momentum by 1ħ. Because we are interested in the most probable transitions, multiple photon absorptions will not be considered. Thus, $\Delta J = \pm 1\hbar$ in all nuclear transitions relevant to our investigation. Consider the interaction between the nucleus with initial angular momentum J and a photon with momentum q:

$$\underline{J} \cdot \underline{q} = \hbar \, m_j \, q \tag{2.8}$$

There are as many scenarios as there are m_j states. Angular distribution of the re-emitted gamma-ray is governed by the original orientation of the nucleus. Angular distributions do not necessarily add coherently; theoretical investigation of this general problem is outside of the scope of this work.

The scenario is significantly simpler for the ground state of the nucleus where J = 0. In this state, each gamma absorbed undergoes the same process. As such, all nuclei behave the same, and there is no nucleus-to-nucleus variation in angular distribution of outgoing radiation. A ground-state angular momentum of zero can only be achieved if there is an even number of protons and neutrons in the nucleus, which is referred to as an even-even nucleus.

Lead 206 is an even-even nucleus containing 82 protons and 82 neutrons. Other even-even nucleus materials of interest include U238.

The J=0 to J=1 transition emits a photon with an angular momentum of 1 as the nucleus returns to the J=0 state. Thus, the angular dependence of the outgoing radiation is that of a dipole. The angular distribution is described as (ref 12):

$$\frac{4}{9\pi^2}\left(1+\frac{1}{2}\mathrm{P}_2(\mathrm{Cos}(\theta))+\frac{1}{4}\pi\mathrm{Cos}(2\phi)\mathrm{P}_2^2(\mathrm{Cos}(\theta))\right) \tag{2.9}$$

Where the π inside of the formula is parity and P_2^2 and P_2 are the original and associated Legendre polynomials respectively. The formula has been normalized such that the integral over all possible directions gives 1.

Formula (2.5) gives the energy dependence of NRF and is suitable for predicting the probability of absorption due to NRF. The combination of equation (2.5) and equation (2.8) yields the probability of scattering gamma in polar coordinates:

$$\sigma_{\mathrm{NRF}}(\mathrm{E},\theta,\phi)=\sigma_0*\frac{1}{\sqrt{\pi}\delta_{\mathrm{NRF}}}\mathrm{e}^{-((\mathrm{E}-\mathrm{E}_0)/\delta)^2}*\frac{4}{9\pi^2}\left(1+\frac{1}{2}\mathrm{P}_2(\mathrm{Cos}(\theta))+\frac{1}{4}\pi\mathrm{Cos}(2\phi)\mathrm{P}_2^2(\mathrm{Cos}(\theta))\right) \tag{2.10}$$

2.4 Compton scattering of electrons

Compton scattering is an example of non-elastic scattering. Consider unpolarized photon scattering first. The Compton formula calculates the difference in the photon's wavelength before and after the scattering with respect to the angle of scattering:

$$\lambda'-\lambda=\frac{\mathrm{h}}{\mathrm{m_e c}}(1-\cos(\theta)) \tag{2.11}$$

We rewrite this equation in terms of the energy of the incident and scattered photon:

$$\mathrm{E}=\frac{\mathrm{hc}}{\lambda}$$

$$E' = \frac{E * m_e c^2}{m_e c^2 + (1 - \cos(\theta))E} \tag{2.12}$$

This allows us to estimate the energy of down-scattered photons to be approximately 405keV and 262keV at 100 and 150 degrees, respectively. We can simplify the formulas by writing it in terms of the wavenumber, k, which is inversely proportional to lambda:

$$k = E/m_e c^2$$
$$k' = \frac{k}{1 + k(1 - \cos(\theta))}$$
$$\frac{k'}{k} = \frac{1}{1 + k(1 - \cos(\theta))} \tag{2.13}$$

To determine the probability of Compton scattering, we separate the cross section into two terms, one describing the interaction between gamma and unbound electron and the second accounting for the fact that electrons are bound:

$$\frac{d\sigma}{d\Omega} = \sigma K_{KN}(k, k')S(k, \theta, Z) \tag{2.14}$$

$S(k', k, \theta, Z)$ is the atomic form factor and takes into account that scattering is done to a bound electron. This is computed numerically in (ref. 13) and interpolated from for our computations. $\sigma K_{KN}(k, k')$ is the Klein-Nishina cross-section formula.

We can include the polarization of incident gamma-rays into the description as shown by (ref. 14):

$$\sigma K_{KN}(\lambda, \lambda') = \frac{r_0^2}{2}\left(\frac{\lambda}{\lambda'}\right)^2 * \left(\frac{\lambda'}{\lambda} + \frac{\lambda}{\lambda'} - 2 + 4(\underline{\varepsilon} * \underline{\varepsilon}')^2\right) \tag{2.15}$$
$r_0 = \frac{e^2}{4\pi\varepsilon_0 mc}$ = classical electron radius

Where the primed and unprimed variables describe the photon before and after scattering and $\boldsymbol{\varepsilon}$ is the direction of polarization. In a polar coordinate system where scattering is at an angle (θ, φ), we can show via trigonometry that:

$$\sigma K_{KN}(\lambda, \lambda') = \frac{r_0^2}{2}\left(\frac{k'}{k}\right)^2 * \left(\frac{k'}{k} + \frac{k}{k'} - 2 + 4(\mathrm{Sin}(\theta)\mathrm{Cos}(\varphi))^2\right) \tag{2.16}$$

Substituting equation (2.16) derived above yields the final expression for the Compton scattering cross section:

$$\frac{d\sigma_{compton}(E,\theta,\phi)}{d\Omega} = S(k,\theta,Z) * \frac{r_0^2}{2} * \left(\frac{1}{1+k(1-\cos(\theta))}\right)^2 * \left(\frac{1}{1+k(1-\cos(\theta))} + 1 + k(1-\cos(\theta)) - 2 + 4(\mathrm{Sin}(\theta)\mathrm{Cos}(\varphi))^2\right) \quad (2.17)$$

This formula describes the Compton scattering that occurs in the witness foil. The directionality of the interaction at this interface is important because we are interested in the probability of scattering the photon into the detector. Compton scattering occurs not only in the foil but at every other stage of the photon's path. Thus, for propagation to the foil and to the detector we need to look at the transmission probability. This can be achieved by integrating (2.17) over all angles because that gives general photon-atom interaction probability. One minus this figure would give the transmission probability. The National Institute of Standards (NIST) website presents tabulated data for Compton scattering-based absorption for all energies and we use it for non-directional, integrated, Compton scattering transmission probabilities (ref. 15).

2.5 Rayleigh scattering of electrons

Rayleigh scattering is an elastic process, i.e., the electron's energy does not change. Hubble's calculations, updated by Fernandez for polarized gammas, yield the formula (ref. 13 and 14):

$$\frac{d\sigma_{Rayleigh}(E,\theta,\phi)}{d\Omega} = F^2(k,\theta,Z) * \frac{r_0^2}{2} * (1 - (\mathrm{Sin}(\theta)\mathrm{Cos}(\varphi))^2) \quad (2.18)$$

Where $F(k,\theta,Z)$ is the atomic form factor, interpolated from Hubble's numerical values.
In the parameter space of the experiment, the Rayleigh scattering cross section is significantly less than the Compton scattering cross section. To the first order, we can disregard Rayleigh scattering in our engineering designs; for parameters such as detector dead time and total energy scattered by the witness foil, Compton scattering and NRF are clearly the dominant processes. Rayleigh scattering and other elastic scattering channels become important when considering the exact portion of the spectrum where NRF occurs. In binning the detector's output in order to consider the NRF bin alone, it is important to account for Rayleigh and nuclear Thomson scattering.

As gamma-ray beams narrow in energy spectrum, elastic scattering processes become relatively more important in comparison to Compton scattering. An ideal beam for NRF would have a width of the nuclear resonance, allowing Compton gammas to be easily discriminated against.

2.6 Nuclear Thomson scattering

Hubbell et al. describe the differential cross section as:

$$\frac{d\sigma_{Thomson}(E,\theta,\phi)}{d\Omega} = \frac{r_0^2}{2} * \left(\frac{Z^2 m_e}{m_{nucleus}}\right)^2 (1 - (Sin(\theta)Cos(\varphi))^2) \quad (2.19)$$

The nucleus of the isotope we use is symmetric, eliminating any concerns over polarization. Furthermore, the nucleus is small in comparison with the gamma's wavelength. Therefore, we do not need to consider the inter-nucleus distributions of particles; this allows us to model the nucleus as a sphere and disregard nuclear form factors. As was the case with Rayleigh scattering of electrons, nuclear Thomson scattering is not a dominant scattering channel. As such, it is relevant only when considering the areas close to NRF on the spectrum.

2.7 Miscellaneous scatterings: Delbrück, pair production

Electron-positron pair production is facilitated by a nuclear field. Gamma-rays interact with the field to create two particles. The positron annihilates with an atomic electron, creating two photons with 0.511 MeVs of energy each. The electron typically scatters off locally, because charged particles do not travel far in matter. This process is probable enough to contribute to the total amount of energy deposited in our detector. Additionally, it will affect the dead times of the detectors and the counting rates of the other processes. In real life, however, 0.511 MeV photons (from positrons) can be easily discriminated against and removed from all calculations and decision metrics.

Delbrück scattering is a result of the interaction between the incident photon and the nucleus's electromagnetic field. Analytical solutions for all energies have not been calculated; it is typically necessary to approximate some energy ranges. On its own, Delbrück scattering occurs with a probability similar to the other scattering channels discussed previously. It is necessary to include for a mathematically complete description of photon-matter interactions. Although including it would be straightforward because it would be an additional coherent scattering channel, it is challenging to prove the veracity of approximations used to correctly describe Delbrück scattering in the parameter space considered. Therefore, our theory, experiment, and engineering designs do not account for Delbrück scattering.

2.8 Gamma-rays and the object under investigation

Half of the experiments were performed with an unobstructed beam hitting the witness foil. The other half was performed using a lead brick as a stand-in for the object under investigation. The isotope of interest in these experiments was Lead 206. As per the summation in equation 2.5a, we need to add NRF scattering channels, because natural lead is purely the Lead 206 isotope. Combining this consideration with equation 2.1 and equation 2.5a yields:

$$\frac{N(L_{brick})}{N(0)} = Exp(-(\mu_{NRF}(E) + \mu_{NON-NRF}(E))L_{brick})$$
$$\mu_{NRF}(E) = \sigma_{NRF}(E) f_{206} n_{Lead}$$
$$\mu_{NON-NRF}(E) = \Sigma\sigma_i(E) n_{Lead} \quad (2.20)$$

$f_{206} = .24$ - fraction of Lead 206 in natural lead
$n_{Lead} = 1.134 * 10^4$ kg/m^3 - density of natural lead
$L_{Brick} = 4.9 * 10^{-2}$m - thickness of the brick
$\sigma_i(E)$ - i-th scattering channel cross section (NRF excluded)
$\sigma_{NRF}(E)$ - NRF cross section from equation 2.6

Equation 2.7 does not take angular considerations into account; photons absorbed through a nuclear resonance process are thought to be scattered and absent from the experiment. We do not track the photon because the probability of its re-entrance into the beam is extremely low, as discussed in Section 2.1.

2.9 Gamma-rays and air

Consider equation 2.5 and equation 2.3. To begin, we define the density of air to be 1.225 kg/m^3. The molar masses and molar fractions of the constituents are used to calculate the average molar mass of the mixture. We use this data, the density of the air, and the molar fractions to determine the concentrations of the constituents. Finally, the NIST website reports the cross sections[1].

[1] It is necessary to double the reported cross-sectional values for diatomic molecules such as oxygen and nitrogen.

	Molar Fraction	Molar Mass, $(\frac{g}{mole})$	n_i (m^{-3})	σ_i (m^2)	$\sigma_i * n_i$ (m^{-1})
N_2	.78	28	$2 * (1.99 * 10^{25})$	$1.20 * 10^{-28}$	0.00475
O_2	.21	32	$2 * (5.35 * 10^{24})$	$1.37 * 10^{-28}$	0.00146
Ar	.01	40	$2.55 * 10^{22}$	$1.78 * 10^{-28}$	0.0000453
Air	1	29			0.00626

Table 2.2. Air constituents and their calculated concentrations and cross sections at 5.9 MeV. (ref. 15 and 17)

The concentration of air is calculated by summating the concentrations of the constituents of air, i.e., nitrogen, oxygen, and argon. According to equation (2.3) it is

$$\mu_{air} = (\Sigma \sigma_i n_i)_{air} \simeq 0.00626$$
$$\frac{N(L_{air})}{N(0)} = e^{-\mu_{air} L_{air}} \quad (2.21)$$

It is necessary to use formulas (2.21) both before and after the witness foil.

2.10 Gamma-rays and the witness foil

When considering the interaction of gamma-rays with the witness foil, it is important to account for (1) transmission of the ray through a portion of the foil, (2) scattering of the ray at the angle of the detector, and (3) transmission of the ray out of the witness foil after scattering (Figure).

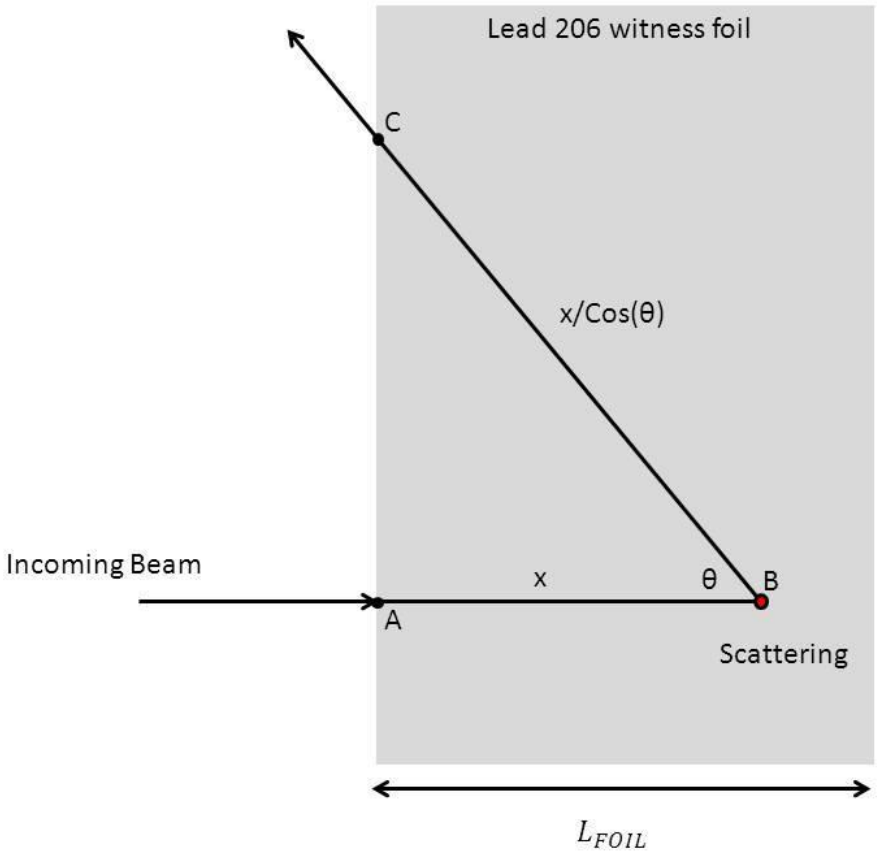

Figure 2.2. Beam evolution through the foil. Beam degrades due to all absorptions (AB), scatters at point B, and goes out losing intensity along (AC).

Flux degradation along AB follows formula (2.10) with the path length denoted as x:

$$N(E)/N_0 = \mathrm{Exp}(-(\mu_{NRF} + \mu_{NON-NRF})x)$$
$$\mu_{NRF} = \sigma_{NRF}(E) f_{206} n_{Lead}$$
$$\mu_{NON-NRF} = \Sigma\sigma_i(E)\, n_{Lead} \quad (2.22)$$

If NRF occurs at point B, NRF is impossible along the path BC due to a recoil energy downshift in the scattered gamma-ray:

$$N(E)/N_0 = \mathrm{Exp}(-\mu_{NON-NRF} x/\mathrm{Cos}(\theta))) \quad (2.23a)$$

If any other scattering event occurs at B, NRF is possible along BC, and the beam degradation formula (equation 2.13) must be updated for a different length:

$$N(E)/N_0 = \mathrm{Exp}(-(\mu_{NRF} + \mu_{NON-NRF})x/\mathrm{Cos}(\theta)) \quad (2.23b)$$

In the first scenario, total beam degradation occurs due to absorption. This is described by a combination of equation 2.22 and equation 2.23:

$$N(E)/N_0 = \mathrm{Exp}(-(\mu_{NRF} + \mu_{NON-NRF}(1 + 1/\mathrm{Cos}(\theta))x) \quad (2.24a)$$
$$N(E)/N_0 = \mathrm{Exp}(-(\mu_{NRF} + \mu_{NON-NRF})x(1 + 1/\mathrm{Cos}(\theta)) \quad (2.24b)$$

Equations 2.24a and 2.24b describe the photon loss along the beam path in the witness foil. If there is no NRF scattering at the turning point of the beam (scenario b), there are absorption losses due to all processes during both legs of the journey (AB and BC). If there is an NRF event at point B, then the second leg of the journey (BC) is via non-NRF channels only, i.e., there is no loss in photons to NRF along BC.

At point B, both nuclear resonance fluorescence (2.10) and other scattering mechanisms (sum of (2.17), (2.18), and (2.19)) can occur:

$$\sigma_{NRF}(E,\theta,\phi) = \sigma_0 * \frac{1}{\sqrt{\pi}\delta_{NRF}} e^{-((E-E_0)/\delta)^2} * * \frac{4}{9\pi^2}\left(1 + \frac{1}{2}P_2(\mathrm{Cos}(\theta)) + \frac{1}{4}\pi\mathrm{Cos}(2\phi)P_2^2(\mathrm{Cos}(\theta))\right)$$
$$\sigma_{NON-NRF}(E,\theta,\phi) = \sigma_{Compton}(E,\theta,\phi) + \sigma_{Rayleigh}(E,\theta,\phi) + + \sigma_{Thompson}(E,\theta,\phi) \quad (2.25)$$

We can determine the probability of scattering by substituting the above expression into equation (2.2):

$$\frac{dN(E,\theta,\phi)}{dx} = -N(E,\theta,\phi)\,(\sigma_{NRF}(E,\theta,\phi)\,f_{foil} + \sigma_{NON-NRF}(E,\theta,\phi))\,n_{Lead}$$
$$\frac{dN(E,\theta,\phi)}{N(E,\theta,\phi)} = -(\mu_{NRF}^{FOIL} + \mu_{NON-NRF})dx$$

The fraction of NRF-capable lead in the foil is different from the fraction in the brick. To distinguish these parameters from each other, we use different "μ" parameters for the foil and the object under investigation.

Applying equation (2.24a) or (2.24b) to the equation we defined for the probability of scattering, we then integrate to compute the complete flux reduction through the slab. If NRF occurs:

$$\frac{dN(E,\theta,\phi)}{N(E,\theta,\phi)} = -\mu_{NRF} e^{-(\mu_{NRF} + \mu_{NON-NRF}(1+1/\mathrm{Cos}(\theta))x)} dx$$

$$\mathrm{Ln}\left(\frac{N_{out}}{N_{in}}\right) = \frac{\mu_{NRF}^{FOIL}}{\mu_{NRF}^{FOIL} + \mu_{NON-NRF}(1 + 1/\mathrm{Cos}(\theta)}\left(e^{-(\mu_{NRF}+\mu_{NON-NRF}(1+1/\mathrm{Cos}(\theta))L)} - 1\right)$$

$$\frac{N_{in}}{N_{out}} = \mathrm{Exp}\left(\frac{\mu_{NRF}^{FOIL}}{\mu_{NRF}^{FOIL} + \mu_{NON-NRF}(1 + 1/\mathrm{Cos}(\theta)}\left(1 - e^{-(\mu_{NRF}+\mu_{NON-NRF}(1+1/\mathrm{Cos}(\theta))L)}\right)\right) \quad (2.26a)$$

Whereas, if a different scattering process happens:

$$\frac{dN(E,\theta,\phi)}{N(E,\theta,\phi)} = -\mu_{NRF}^{FOIL} e^{-(\mu_{NRF}+\mu_{NON-NRF})(1+1/\mathrm{Cos}(\theta))x)} dx$$

$$\mathrm{Ln}\left(\frac{N_{out}}{N_{in}}\right) = \frac{\mu_{NON-NRF}}{(\mu_{NRF}^{FOIL} + \mu_{NON-NRF}) * (1 + 1/\mathrm{Cos}(\theta)}\left(e^{-(\mu_{NRF}+\mu_{NON-NRF})(1+1/\mathrm{Cos}(\theta))L)} - 1\right)$$

$$\frac{N_{in}}{N_{out}} = \mathrm{Exp}\left(\frac{\mu_{NON-NRF}}{(\mu_{NRF}^{FOIL} + \mu_{NON-NRF}) * (1 + 1/\mathrm{Cos}(\theta)}\left(1 - e^{-(\mu_{NRF}+\mu_{NON-NRF})(1+1/\mathrm{Cos}(\theta))L)}\right)\right) \quad (2.26b)$$

2.11 Gamma-rays and the Compton filters

After the gamma-ray hits the witness foil, it continues to travel through additional air space before it encounters the lead and copper filters before the detectors. These filters are thin (3mm thick) sheets of metal and preferentially scatter lower-energy photons. For the natural lead filter, scattering is described similarly to equation 2.20, which described scattering at the lead brick:

$$\frac{N_{in}}{N_{out}} = e^{-(\mu_{NRF}(E)+\mu_{NON-NRF}(E))L_{\text{Lead Filter}}} \quad (2.27)$$

For the copper filter, scattering is the same at the lead filter but without NRF:

$$\frac{N_{in}}{N_{out}} = e^{-\mu_{copper}(E)L_{\text{Copper Filter}}} \quad (2.28)$$

Equations (2.27) and (2.28) describe the energy dependence of attenuation of the beam. Sub-MeV photons that underwent Compton scattering in the witness foil are sharply attenuated, while multi-MeV photons from elastic processes are almost never scattered. This decreases the noise reaching the detector and the dead time. Additionally, it helps with factors described in the next sections.

2.12 Putting it all together: Flux on detector

To begin, consider the beam described in equation 2.1:

$$\Phi(E) = \Phi_0 * \frac{1}{\sqrt{\pi} * \delta} e^{-((E-E_0)/\delta)^2}$$

The beam then hits the object under investigation (equation 2.11). The "brick in" scenario will define the length of the brick as measured, while the "no brick" scenario resulting in an unobstructed beam will be modeled by setting the length to zero.

$$\frac{N_{in}}{N_{out}} = e^{-(\mu_{NRF}(E)+\mu_{NON-NRF}(E))L_{brick}}$$

Next, the beam propagates through air until it hits the witness foil (2.21), where it attenuates by:

$$\frac{N_{in}}{N_{out}} = e^{-\mu_{air}L_{air}}$$

Scattering in the foil is governed by equation (2.26a) when NRF is present, and by equation (2.26b) when NRF is not present:

$$\frac{N_{in}}{N_{out}} = Exp\left(\frac{\mu_{NRF}^{FOIL}}{\mu_{NRF}^{FOIL} + \mu_{NON-NRF}(1 + 1/Cos(\theta)}(1 - e^{-(\mu_{NRF}+\mu_{NON-NRF}(1+1/Cos(\theta))L_{FOIL})})\right)$$

$$\frac{N_{in}}{N_{out}} = Exp\left(\frac{\mu_{NON-NRF}}{(\mu_{NRF}^{FOIL} + \mu_{NON-NRF}) * (1 + 1/Cos(\theta)}(1 - e^{-(\mu_{NRF}+\mu_{NON-NRF})(1+1/Cos(\theta))L_{FOIL})})\right)$$

After interacting with the witness foil, the beam then interacts with more air (2.12), more natural lead (Compton filter) (2.27), and lastly copper (Compton filter) (2.28)

$$\frac{N_{in}}{N_{out}} = e^{-\mu_{air}(E)\,L_{air}} * e^{-\mu_{copper}(E)L_{Copper\ Filter}} * e^{-(\mu_{NRF}(E)+\mu_{NON-NRF}(E))L_{Lead\ Filter}}$$

Combining these interactions, a formula for total attenuation of the beam:

$$\frac{\Phi(E)}{\Phi_0} = \frac{1}{\sqrt{\pi} * \delta} e^{-((E-E_0)/\delta)^2} e^{-\mu_{air}(E)\,L_{air}} e^{-\mu_{copper}(E)L_{Copper\ Filter}}$$
$$* e^{-(\mu_{NRF}(E)+\mu_{NON-NRF}(E))(L_{Lead\ Filter}+L_{brick})} *$$
$$* [Exp\left(\frac{\mu_{NRF}^{FOIL}}{\mu_{NRF}^{FOIL} + \mu_{NON-NRF}(1 + 1/Cos(\theta)}(1 - e^{-(\mu_{NRF}+\mu_{NON-NRF}(1+1/Cos(\theta))L_{FOIL})})\right) +$$
$$+ Exp\left(\frac{\mu_{NON-NRF}}{(\mu_{NRF}^{FOIL} + \mu_{NON-NRF}) * (1 + 1/Cos(\theta)}(1 - e^{-(\mu_{NRF}+\mu_{NON-NRF})(1+1/Cos(\theta))L_{FOIL})})\right)]$$

(2.29)

L_{air},$L_{Copper\ Filter}$, and $(L_{Lead\ Filter} + L_{brick})$ are the total distances the beam travels in air, copper, and lead, respectively. The term inside the square brackets describes the beam's travel in the witness foil. The cross sections outside the witness foil are taken from the NIST website (ref. 15) and are interpolated for energy dependence.

Scattering is a probabilistic process in nature that occurs on a photon-by-photon basis. In our simplified description, we ignore multiple scattering events during attenuation. Therefore, we can combine the terms for the photon's travel length in air before and after interaction with the witness foil. Photons that are absorbed by air disappear. That is, we do not need to reshape the spectrum but instead attenuate it. A similar stochastic argument is used to add equations (2.26a) and (2.16b) in the square brackets.

2.13 Gamma-rays and the high-purity germanium detector

Several events occur in the detector. We will cover complete vs. incomplete gamma-ray energy deposition, detector and electronics dead times, proper peak fitting to account for secondary absorption effects, and the effects of random DC offset voltage changes.

Gamma-rays interact with the detector and in the process deposit energy onto it. The energy that is deposited is converted into an electron-hole pair in the semiconductor. When this happens, the detector collects, amplifies, and tallies the total charge generated in the detecting medium. This charge number is recorded in either a histogram format (GENIE) or as a combination of the charge number with the timestamp of the event (CODA).

The interaction between the gamma-rays and the detector is a complicated multi-scattering process; a complete and accurate model of this interaction is outside the scope of this work. Ideally, the photon loses all its energy during multiple collisions inside the detecting medium. This is referred to as "complete capture" of the photon by the detector. The energy loss is represented by the number of electron-hole pairs created. The multi-scatter process is thought to occur inside a sphere of a certain radius. This radius characterizes the combined distance traveled by the photon as it "random walks" through multiple scatterings. The detecting medium must be significantly larger than the characteristic radius such that the majority of gammas that are captured undergo complete capture. In this ideal scenario, photon energy is accurately deduced from the total charge detected.

Incomplete capture can occur when capture begins too close to the surface of the detecting medium. The gammas rays' movement is described by a multi-scattering random walk, causing it to "bounce" off of the detector before it has a chance to deposit all of its energy. To describe

this phenomenon mathematically, consider the volume over which complete capture happens versus the volume over which incomplete capture happens. This loss of capacity to correctly detect gamma-ray flux is both geometry- and energy-dependent because the characteristic radius for a multi-scatter random walk depends on energy. The amount of capture that occurs is one of the contributing factors to the detector efficiency.

The detector efficiency profile curve is unique to each detector. It defined by the probability of detecting a gamma-ray as an event at the appropriate energy. These curves are determined by geometry, the material constituting the detecting medium, specific detector peculiarities, and other detector variations. The shape of the curve is hypothesized to be identical for all detectors of the same type and design. Absolute magnitude of the curve is determined from calibration runs. We measure detector efficiency at a given point in the energy spectrum in order to scale the efficiency curve to produce absolute efficiency. This aids in the process of reconstructing the incident spectrum from the detected spectrum.

Spectroscopy—the study of energy spectrums—is at its core a single photon counting process. In other words, each event recorded must be a record of a single gamma-ray interacting with the detector; incidents where two gamma-rays hit the detector nearly simultaneously and are counted as one are highly undesirable. For this reason, HPGe detectors have a "dead time," which is a time where the detector collects and analyzes the charge created by the gamma-ray. The detector collects charge from one or more events and produces an output voltage pulse. The ADC has a dead time in processing this voltage signal. Secondary dead time arises from the software recording the event. The Genie software records energy only and has a significantly shorter dead time than the software CODA which records complete information on each event. Each gamma detected induces the system to stop and record for a length of time on the order of microseconds. Calibration and background runs are usually performed to set the dead time to be as close to zero as possible, while production runs can have significant dead time fractions. The dead time fraction naturally affects how many gammas are detected. A dead time fraction of 50% would mean that the counting rates that are recorded are only half as many as those predicted.

Correction for dead time is achieved through careful comparison of background peak strength between production runs and background runs. Consider a run during which we detect a total of N events across the whole spectrum and n events in the bin of interest. The time of the run is denoted by T, and dead time per event is denoted by τ. Total dead time is then N *τ. The fraction of particles that we cannot detect in any beam due to dead time is N * τ / T. To calculate the real value of n, we must add that fraction back:

$$n_{real} = n\left(1 + N\frac{\tau}{T}\right)$$
$$r_{real} = \frac{n_{real}}{T} = \frac{n}{T}(1 + N\frac{\tau}{T}) = r(1 + R\tau) \quad (2.30)$$

The real rate, particles per unit time, is the same for the background peaks during all runs. It is easy to show that during background runs,

$$R\tau << 1 \qquad (2.31)$$

R is inferred from the total number of events recorded and the length of the run. T can be overestimated at 20 microseconds. According to condition 2.31, background runs provide the real rates of the background peaks. We can compare these to the rates recorded during the production runs. The ratio determines the factor needed to compensate for dead time. A more complete analysis cross-compares rates to infer τ and analyzes the time to determine a functional form for $\tau(E)$. However, to the first order, the ratio approach is sufficient.

How does one determine peak strength? Before we answer this question, let us first introduce a few more notations. The output of the detector is represented as a histogram where each bin is set to be of a certain width (usually a few KeVs). Resolution concerns set the width limit. To define a lower bin width is useless because stochastic fluctuations in the output make zooming in along the energy axis meaningless past a certain level. We will call x the bin number and y the number of counts in that bin. To the first order, the peak is a Gaussian of width σ and centered on point c (complete explanation is in ref. 18):

$$y = \text{Constant} * e^{-(x-c)^2/2\sigma^2}$$

If the detector had perfect resolution, the scenario in (citation) would be a delta function. The reality of resolution limitations broadens it to the equation above. However, this effect does not change the area under the Gaussian; therefore, total peak strength is not affected by the width σ. Every gamma recorded in the histogram is still from the peak. Stochastic fluctuations only broaden the peak (as in Doppler broadening of NRF, discussed above). Thus, the area under the Gaussian is representative of the area of the peak as it is emitted. Unfortunately, there are two additional effects that detract from the area under the Gaussian and cannot be captured by a simple Gaussian fit because it would misrepresent the true number of gammas in the peak.

Incomplete charge collection can occur due to "trapping of charge" by impurities, voids, and other lattice defects. Detectors are irradiated, causing further defects in addition to the ones from the manufacturing process. Perfect resolution detectors give an exponential tail on the left side of the peak. To represent this realistically, it is necessary to convolve an exponential term with the Gaussian representing the resolution:

$$y = \text{Constant} * e^{\frac{x-c}{\beta}} * \text{ERFC}\left(\frac{x-c}{\sqrt{2}\sigma} + \frac{\sigma}{\sqrt{2}\beta}\right)$$

This equation is referred to as a "skewed" Gaussian where β is a measure of "skewedness." The second correction comes from multiple low-angle Comptons and from losing electrons created in the gamma absorption process. These effects remove gammas from the peak's bins and shift the peak toward the left on the histogram, adding to the background. A perfect resolution detector represents these effects as a step function:

$$y = \text{Constant} * \text{ERFC}(\frac{x - c}{\sqrt{2}\sigma})$$

A combined fit function of the detector is represented mathematically by:

$$y = \text{Constant} * (e^{-(x-c)^2/2\sigma^2} + \text{ERFC}\left(\frac{x-c}{\sqrt{2}\sigma}\right) + e^{\frac{x-c}{\beta}} * \text{ERFC}(\frac{x-c}{\sqrt{2}\sigma} + \frac{\sigma}{\sqrt{2}\beta}) \quad (2.32)$$

This fit function accounts for some of the gammas that are lost due to various effects.
A final concern to be aware of while analyzing the data is random DC offset changes. Each gamma detected is represented by a total charge number of electrons collected. A DC offset effect causes the charge number to change, which shifts the x-axis of the histogram for the remainder of the experiment. Careful assessment of each peak from run to run ensures that the offset remains constant between runs. If the offset differs from run to run, the x-axis must be shifted to allow for correct addition of the histograms.

The data analysis process consists of the following steps:

- Calibrate the x-axis of each experimental run to ensure that it is offset correctly
- Normalize by the time of the run to calculate count rates
- Fit the background peaks using equation (2.32)
- Compute and apply dead time corrections via equations (2.30 and 2.31)
- Add together the runs with the same conditions (brick in/out, angles, etc.)
- Calibrate the x-axis using background lines
- Fit NRF peaks
- Fit the first escape NRF peaks

Calibration of the histogram's energy axis is performed using known energies of background peaks. The Th232 decay chain is particularly abundant in detectable peaks. The concrete constituting walls, floors, and ceiling contains these peaks, supplying us with multiple reference points. It is necessary to compare the relative strengths of these peaks to ensure that they are consistent with values from literature. This ensures correct peak identification. The highest detectable peaks are the two 0.511 MeV gammas produced from electron-positron annihilation.

Potassium 40 from the concrete, and Cobalt 60 from neutron irradiation of steel in rebar in concrete peaks, are also detectable. This multitude of energies with specific lines in the spectrum enables unambiguous calibration computations.

The first escape peak occurs due to the gamma-rays participating in the pair production event. The positron created annihilates to produce 2 gammas with 0.511MeV of energy. The first escape peak is the peak of the event where one of these gammas escapes. The second escape peak is the event where both annihilation gammas escape from the detector.

Backscatter peaks from the experimental chamber need to be identified. We will account for the 180° Compton scattering from the back wall into the detector.

2.14 Theory conclusion: flux vs. the angle for main scattering channels

In this chapter we considered the source beam, its interaction with various materials and objects, the interaction between the beam and the detector, detector physics as pertained to data analysis, and the statistics of processes described.

The source beam from HIγS is characterized to be Gaussian in energy (2.1):

$$\Phi(\mathrm{E}) = \Phi_0 * \frac{1}{\sqrt{\pi} * \delta} \mathrm{e}^{-((\mathrm{E}-\mathrm{E}_0)/\delta)^2}$$

An analytical model for beam evolution through the experiment is illustrated mathematically by equation (2.29):

$$\frac{\Phi(\mathrm{E})}{\Phi_0} = \frac{1}{\sqrt{\pi} * \delta} \mathrm{e}^{-((\mathrm{E}-\mathrm{E}_0)/\delta)^2} \mathrm{e}^{-\mu_{\mathrm{air}}(\mathrm{E})\, \mathrm{L}_{\mathrm{air}}} \mathrm{e}^{-\mu_{\mathrm{copper}}(\mathrm{E}) \mathrm{L}_{\mathrm{Copper\ Filter}}}$$
$$* \mathrm{e}^{-(\mu_{\mathrm{NRF}}(\mathrm{E})+\mu_{\mathrm{NON-NRF}}(\mathrm{E}))(\mathrm{L}_{\mathrm{Lead\ Filter}}+\mathrm{L}_{\mathrm{brick}})} *$$
$$* \left[\mathrm{Exp}\left(\frac{\mu_{\mathrm{NRF}}^{\mathrm{FOIL}}}{\mu_{\mathrm{NRF}}^{\mathrm{FOIL}} + \mu_{\mathrm{NON-NRF}}(1 + 1/\mathrm{Cos}(\theta)}\left(1 - \mathrm{e}^{-(\mu_{\mathrm{NRF}}+\mu_{\mathrm{NON-NRF}}(1+1/\mathrm{Cos}(\theta))\mathrm{L}_{\mathrm{FOIL}})}\right)\right) + \right.$$
$$\left. \mathrm{Exp}\left(\frac{\mu_{\mathrm{NON-NRF}}}{(\mu_{\mathrm{NRF}}^{\mathrm{FOIL}} + \mu_{\mathrm{NON-NRF}}) * (1 + 1/\mathrm{Cos}(\theta)}\left(1 - \mathrm{e}^{-(\mu_{\mathrm{NRF}}+\mu_{\mathrm{NON-NRF}})(1+1/\mathrm{Cos}(\theta))\mathrm{L}_{\mathrm{FOIL}})}\right)\right)\right]$$

The probability of detection is inferred in equation 2.21and is further described by the data analysis approach.

Chapter 3: Experimental verification of the angular dependencies for the polarized gamma-ray scattering channels

In this chapter, we describe our experiment at Triangle University National Laboratory's High Intensity Gamma-Ray Source (HIγS). Data acquisition and analysis are presented and discussed. The experiment consisted of four successive production runs.

The first production run had the HIγS beam unobstructed and detectors positioned in a vertical plane (φ=90). The second production run had a brick in the beam, while the detector setup was still vertical. The third and fourth runs repeated the measurements of the first two, with detectors positioned in the horizontal plane. Table 3.1 shows the production run parameters.

Run Number	φ	BRICK
1	90	Out
2	90	In
3	0	Out
4	0	In

Table 3.1. Production run parameters.

3.1 High Intensity Gamma-Ray Source (HIγS) beam, shielding, and beam monitoring

A gamma-ray beam is created by free-electron laser (FEL) laser light upscattering of electrons. The exact beam rep rate is not significant because the detector readout rate is the limiting factor. The beam is considered to be around 10^8photons per second total, with energy centered on 5.9 MeV and energy spread (1/e) of 200 keV. The beam is extremely stable and has been used for characterization of NRF resonances (19). In fact, Lead 206 has been characterized here in 2011 (20). Every run started with a quick energy-spectrum measurement performed by a zero degree detector. This detector (detector 5) was moved onto the beam path *after* all the collimators, experimental equipment, and so on.

Figure 3.1 shows a scheme of the experimental chambers.

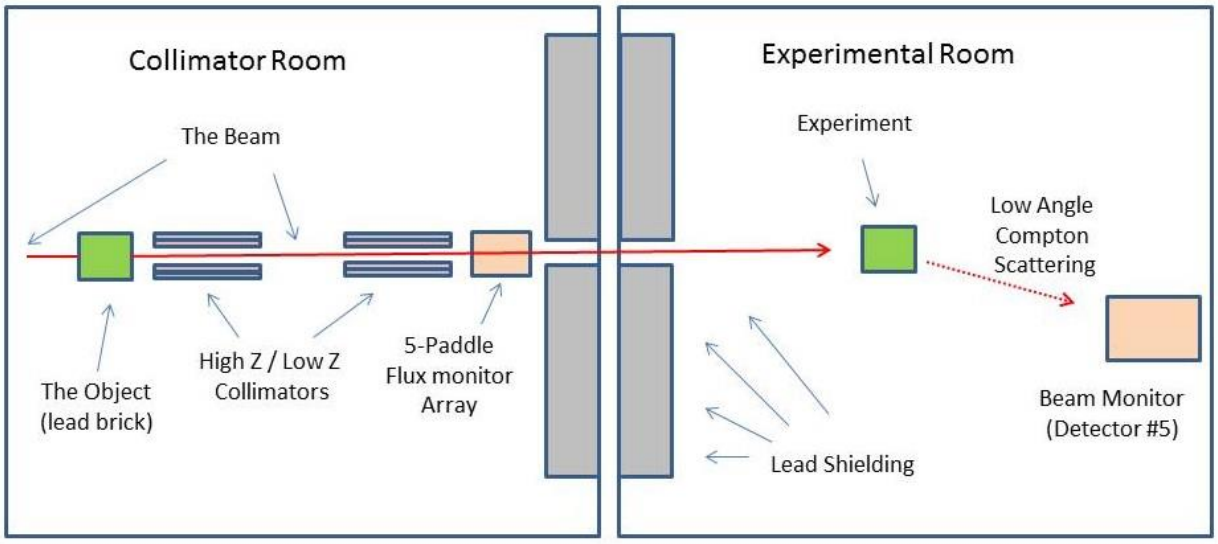

Figure 3.1: Experimental chambers, shielding, and beam flux monitoring.

Two rooms constitute the experimental chamber: the collimator room and the experiment room. The collimator room contains collimators, shielding, a five-paddle flux measuring device, and a place for the object under investigation (which was used in half of the runs). The experimental room contains more shielding, detectors (production detectors number 1, number 2, and number 3, as well as zero degree detector number 5), the scattering foil, and the detector holding rig. The object under investigation (a natural lead brick) was inserted before the final collimator array. This was done in hopes of filtering out low-angle Comptons by the collimator. The ideal collimation setup includes a long (several meters) collimator, followed by an even longer free-flight distance (10 to 20 meters), to be followed by a second long (meters) collimator. The HIγS setup consisted of a single collimator, thought to be sufficient due to low gamma-ray beam divergence.

The collimators themselves are tubes of copper that are inserted into lead tubing surrounded by lead bricks. The lower Z and density material is thus inside the higher Z and density material. This is a typical setup. Lower density means lower probability of multiple small-angle Comptons back into the beam. Thus, the inner tube scrapes off small angles, as we are trying to get divergent gamma to interact once and get scattered outside into the higher Z tube. The higher Z and density material surrounding the primary collimator serves as the final destination for everything that the primary collimator scrapes off. Higher Z is better because it is correlated to density and total absorption cross-section.

Of interest are ways one might get a reading on total flux from experimental runs. We used a five-paddle coincidence system in the collimator room to provide us with a rough estimate of the flux. The five paddles and the processes in them enable counting electronics to discriminate

whether the electron or gamma was triggering, so one can discard electrons. This works very well for an unobstructed beam.

Half of the runs were with the lead brick inside the beam upstream of the collimators, which is the configuration representative of the production scan looking for an isotope of interest. This has an unintended consequence: pair production in the brick introduces too many electrons in the beam for the paddles to work effectively. Each electron shuts the system down, introducing too much dead time to detect gammas correctly.

The zero degree detector (detector 5) was moved to the side of the beam for production runs. It is thought that a reading of that detector can provide us with an idea of how much flux was on the target. Compton scattering into detector 5 from the witness foil should be very well defined because geometry unambiguously determines a downshift in the energy of scattered photons. Thus the production run vs. the background run output of detector 5 should give us a measure of flux on the foil; we just need to look at the specific energies. Figure 3.2 shows detector 5 as seen from the foil placement.

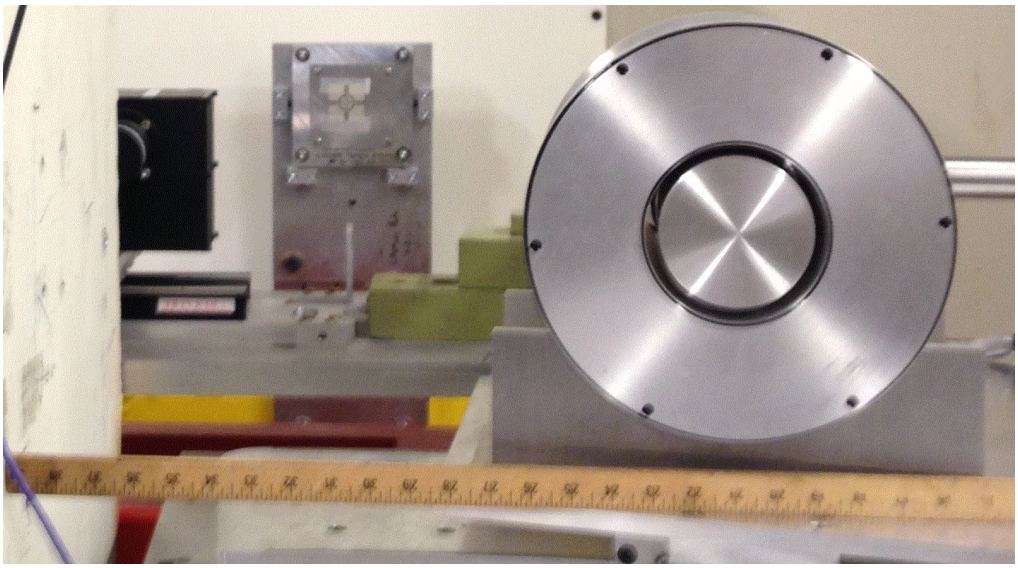

Figure 3.2. Detector 5 offset of the beam path by about 10 inches.

Further positioning calculations place the detector 25 inches downstream. Thus the witness foil -> detector 5 angle is about arctan(10/61), or about 4.7 degrees. This, plugged into the Compton formula from section 2.4, gives us the following:

$$E' = \frac{E * m_e c^2}{m_e c^2 + (1 - \cos(\theta))E} = 5.68\ \text{MeV} \qquad (3.1)$$

The strength of the peak at this energy is representative of the total flux on the target. This peak will provide us with run-to-run total flux on the target normalization to account for the variability in the HIγS beam.

Stacks of standard lead bricks provided shielding in the experimental room.- Figure 3.3 shows the view upstream from the target position in the experimental room into the collimator room.

Figure 3.3. The view upstream from the target. Shielding lead bricks are painted green, and the

HeNE red laser is on for alignment purposes. Red-painted shields on the detectors at a 150-degrees backward angle barely avoid clipping the incoming beam.

Further shielding bricks were stacked behind each detector, to prevent low-angle scattering from the beam into the back of the detectors. This, together with copper/lead housing on the detecting mediums, completes the shielding picture.

To recap: The long collimator in the collimator room was followed by a wall of lead bricks on the inside of the experimental room. Furthermore, lead bricks were protecting the back sides of the detectors. HPGe crystals were housed in copper/lead shielding combinations.

The last line of the defense was the positioning of the experiment inside the experimental room. The experimental room design ensured that the distances to the experiment from the walls,

ceiling, and floors were long enough. The side walls were more than two meters away, while the back wall was significantly farther. The ceiling was fairly high. In nuclear physics, conducting gamma-ray spectral measurements is about controlling and understanding backgrounds. The scatter from physical walls, if not controlled by the geometry of the room itself, could become prohibitively hard to mitigate.

3.2 Witness foil design, composition, and mounting

Natural lead has about 24% of Lead 206 in it. We endeavored to excite Lead 206 resonance, so we obtained a sample that was as isotopically pure as possible. Isoflex (4), a local San Francisco company, provided us with a 90.5% Lead 206 sample. The sample was molded into a thin disk, with a diameter of 1.5 cm and mass of about 2.4 g. We have used the term "witness foil" interchangeably with "the target" during our discussion; both refer to the same object in the picture below.

Figure 3.4. The Lead 206 target from both sides, next to a dime for a scale comparison.

A full isotopic and chemical analysis is in Tables 3.2 and 3.3.

Isotope	Pb-204	Pb-206	Pb-207	Pb-208
Content (%)	0.04	90.5	6.67	2.79

Table 3.2. Isotopic composition of the target.

(Certificate#1606 from ISOFLEX USA - ref.22)

Element	Ag	Al	B	Bi	Ca	Co	Cr	Cu	Fe
Content (ppm)	<3	4	10	<3	<10	<10	<3	<1	10
Element	Mg	Mn	Ni	Si	Sn	Ti			
Content (ppm)	<3	<1	<3	<10	<10	<10			

Table 3.3. Chemical composition of the target.

(Certificate#1606 from ISOFLEX USA - ref.22)

We will neglect chemical impurities in our calculations (a few percent by mass density), while incorporating isotopic impurities (>10%). This has been accounted for in the preceding chapter; we use an isotopic fraction to describe the amount of excitable Lead 206 in the target.
The witness foil needs to be held in place securely during the experiment. The holder needs to be rigid enough to hold the target in place. Another requirement is for the holder not to contaminate the pure signal. Cardboard was stretched perpendicular to the beam, and the target was taped to it. Because organic matter consists mainly of carbon, oxygen, nitrogen, and hydrogen, no nuclear resonances can appear in the spectrum. The Compton scattering and elastic processes are all dependent on the powers of atomic charge, so Z's of 12, 16, 15, and 1 will not distort the spectrum from Z=82 (lead) too much. The thicknesses and densities of holding materials were low enough to ensure that the distortions would be negligible.

3.3 Detectors: backgrounds, calibration, placement, and detector holding rig

High-purity germanium (HPGe) ORTEC detectors were used. Initially, we planned to use four detectors for data collection and the fifth detector for beam monitoring and specification. We assigned numbers 1 through 5 to the detectors to avoid confusion in signal processing. Unfortunately, detector 4 died, leaving us with 1, 2, and 3 as production detectors and 5 as the beam monitor. Following are documentation pages describing the detectors.

QUALITY ASSURANCE DATA SHEET
GMX SERIES GAMMA-X HPGe
(HIGH-PURITY GERMANIUM) COAXIAL PHOTON DETECTOR SYSTEM

MODEL AND SERIAL NUMBERS

Detector Model No. GMX-60230-P-S
Cryostat Configuration PopTop
Dewar Model —
Preamplifier Model 237N
Preamplifier S/N 778
H.V. Filter Model 138
H.V. Filter S/N 8740
Smart-1-N —

IMPORTANT REFERENCE DATA

Ship Date 6-16-10
Serial No. 34-TN31061A

When calling Customer Service, always reference this Detector Serial No.

Dewar Capacity — Static Holding Time — Detector Cool-Down Time —

DIMENSIONS

Detector Diameter 64.5 mm
Detector Length 79.4 mm
End Cap to Detector 4 mm

ABSORBING LAYERS

Beryllium 0.50 mm
Aluminum — mm
Inactive Germanium – 0.3 μm

Recommended Operating Bias, NEGATIVE 3500 V

PERFORMANCE SPECIFICATIONS*

	Warranted	Measured	Amplifier Time Constant
Resolution (FWHM) at 1.33 MeV, ^{60}Co	2.53 keV	2.15 keV	6 μs
Peak-to-Compton Ratio, ^{60}Co	50:1	62:1	6 μs
Relative Efficiency at 1.33 MeV, ^{60}Co	— %	56.0 %	6 μs
Peak Shape (FWTM/FWHM), ^{60}Co	2.00	1.93	6 μs
Peak Shape (FWFM/FWHM), ^{60}Co		2.70	6 μs
Resolution (FWHM) at 5.9 keV, ^{55}Fe	1210 eV	1045 eV	6 μs

*Measured at a nominal rate of 1000 counts/s unless otherwise specified.

Other: Capsule NOCA # 2983
Cryostat PG-1.2-S # 4053

Data Certified by: DJ Wilson Date: 6-15-10

Figure 3.5. Specs for detector 1, detector 2, and detector 3.

GERMANIUM DETECTOR DIAGRAM

SERIAL NUMBER 36-TN31061A

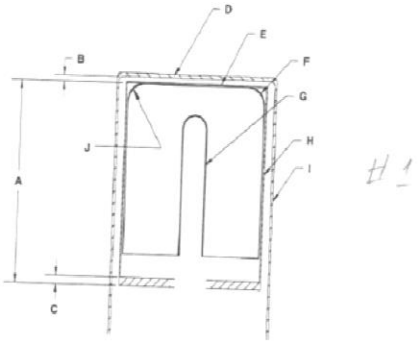

H 1

COMPANY PRIVATE

BASIC DETECTOR DIMENSIONS	
DETECTOR DIAMETER	64.6 mm
DETECTOR LENGTH	80.9 mm
DETECTOR END RADIUS (J)	8 mm, NOMINAL
HOLE DIAMETER	11.2 mm
HOLE DEPTH	72.7 mm
HOLE BOTTOM RADIUS	8 mm, NOMINAL

MISCELLANEOUS DETECTOR ASSEMBLY DIMENSIONS AND MATERIALS			
IDENTIFIER	DIMENSION	DESCRIPTION	MATERIAL(S)
A	105 mm	MOUNT CUP, LENGTH	ALUMINUM
B	4 mm	END CAP TO CRYSTAL GAP	N.A.
C	3.2 mm	MOUNT CUP BASE	ALUMINUM
D	0.5 mm	END CAP WINDOW	BERYLLIUM
E	0.05 mm	INSULATOR/SHEILD	ALUMINIZED MYLAR
F	0.3 microns	OUTSIDE CONTACT LAYER	BORON
G	1300 microns	HOLE CONTACT LAYER	LITHIUM
H	0.76 mm	MOUNT CUP WALL	ALUMINUM
I	1 mm	END CAP WALL	ALUMINUM

ORTEC
801 S. ILLINOIS AVE.
OAK RIDGE TN 37831

Figure F.3

152

Figure 3.6. Geometry specs for detectors 1, 2, and 3.

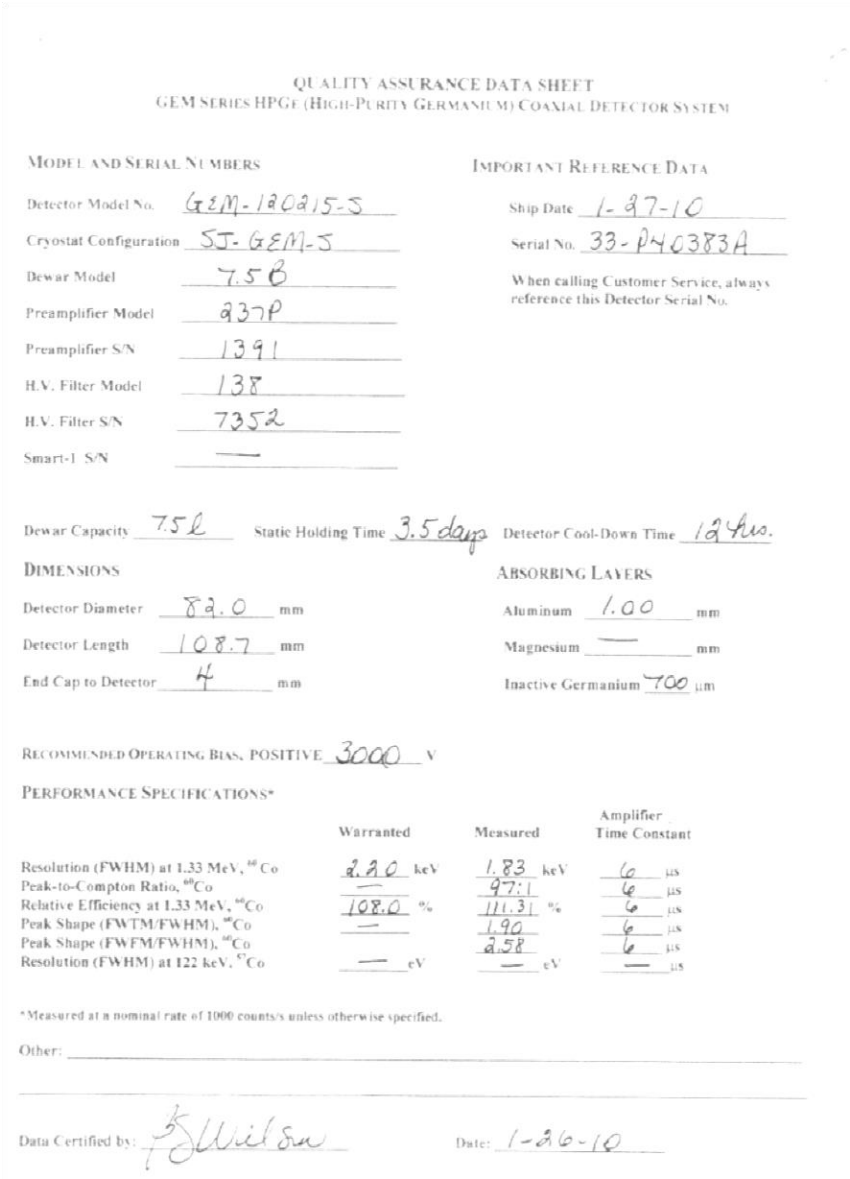

QUALITY ASSURANCE DATA SHEET
GEM SERIES HPGE (HIGH-PURITY GERMANIUM) COAXIAL DETECTOR SYSTEM

MODEL AND SERIAL NUMBERS

Detector Model No. GEM-12P215-S
Cryostat Configuration SJ-GEM-S
Dewar Model 7.5B
Preamplifier Model 937P
Preamplifier S/N 1391
H.V. Filter Model 138
H.V. Filter S/N 7352
Smart-1 S/N —

IMPORTANT REFERENCE DATA

Ship Date 1-27-10
Serial No. 33-P40383A

When calling Customer Service, always reference this Detector Serial No.

Dewar Capacity 7.5 l Static Holding Time 3.5 days Detector Cool-Down Time 12 hrs.

DIMENSIONS

Detector Diameter 82.0 mm
Detector Length 108.7 mm
End Cap to Detector 4 mm

ABSORBING LAYERS

Aluminum 1.00 mm
Magnesium — mm
Inactive Germanium 700 µm

RECOMMENDED OPERATING BIAS, POSITIVE 3000 V

PERFORMANCE SPECIFICATIONS*

	Warranted	Measured	Amplifier Time Constant
Resolution (FWHM) at 1.33 MeV, ^{60}Co	2.20 keV	1.83 keV	6 µs
Peak-to-Compton Ratio, ^{60}Co	—	97:1	6 µs
Relative Efficiency at 1.33 MeV, ^{60}Co	108.0 %	111.3 %	6 µs
Peak Shape (FWTM/FWHM), ^{60}Co	—	1.90	6 µs
Peak Shape (FWFM/FWHM), ^{60}Co		2.58	6 µs
Resolution (FWHM) at 122 keV, ^{57}Co	— eV	— eV	— µs

*Measured at a nominal rate of 1000 counts/s unless otherwise specified.

Other: _____

Data Certified by: J. Wilson Date: 1-26-10

Figure 3.7. Detector specs for detector 5.

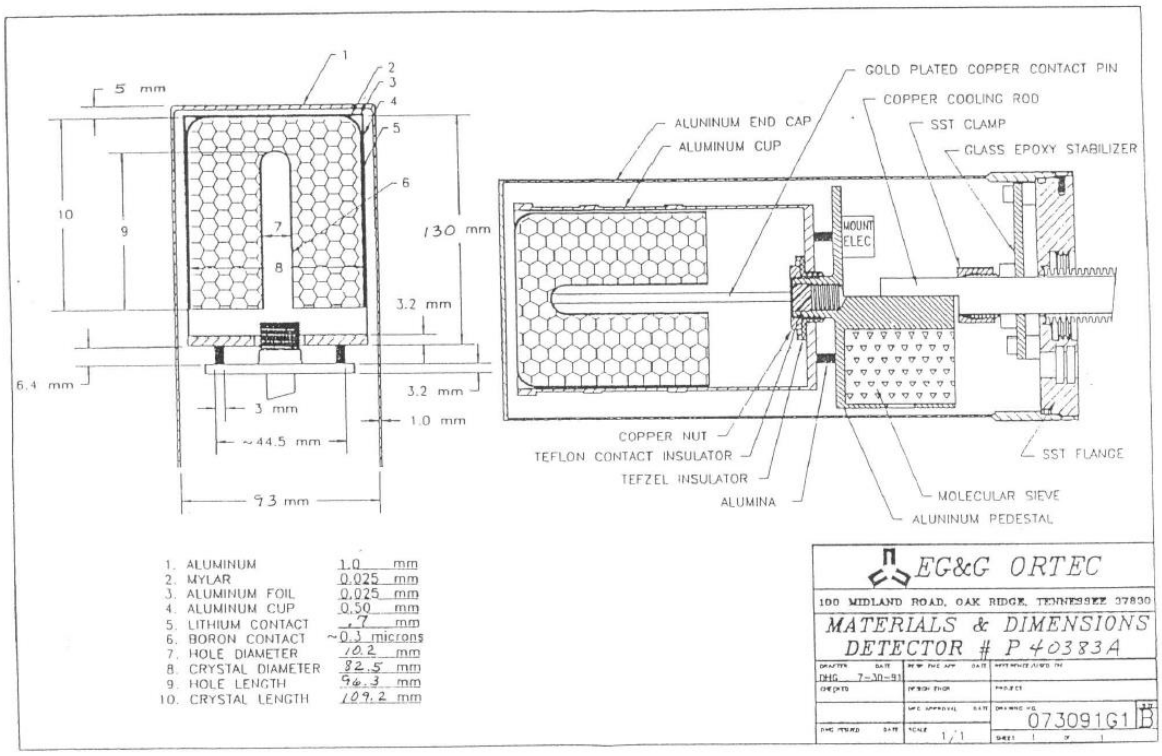

Figure 3.8. Detector geometry specs for detector 5.

With the detectors in position, we took the measurement of the background. Above the 2.6 MeV Tl-208 line, the only source of counts are very infrequent cosmic rays. Following is the total spectrum of the background run for detector 1 (Fig. 3.8). All background peaks are marked in Fig 3.9, which zooms in on the background spectrum.

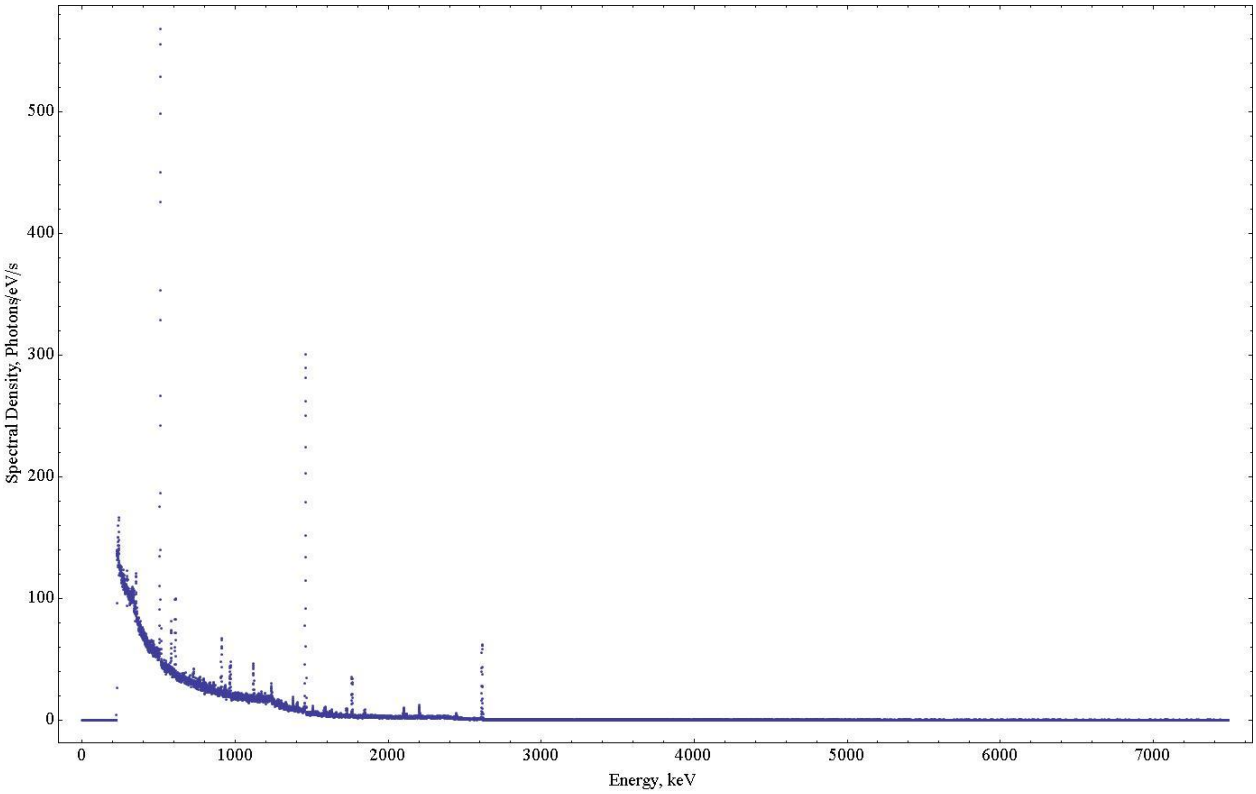

Figure 3.9. Detector 1: Background run.

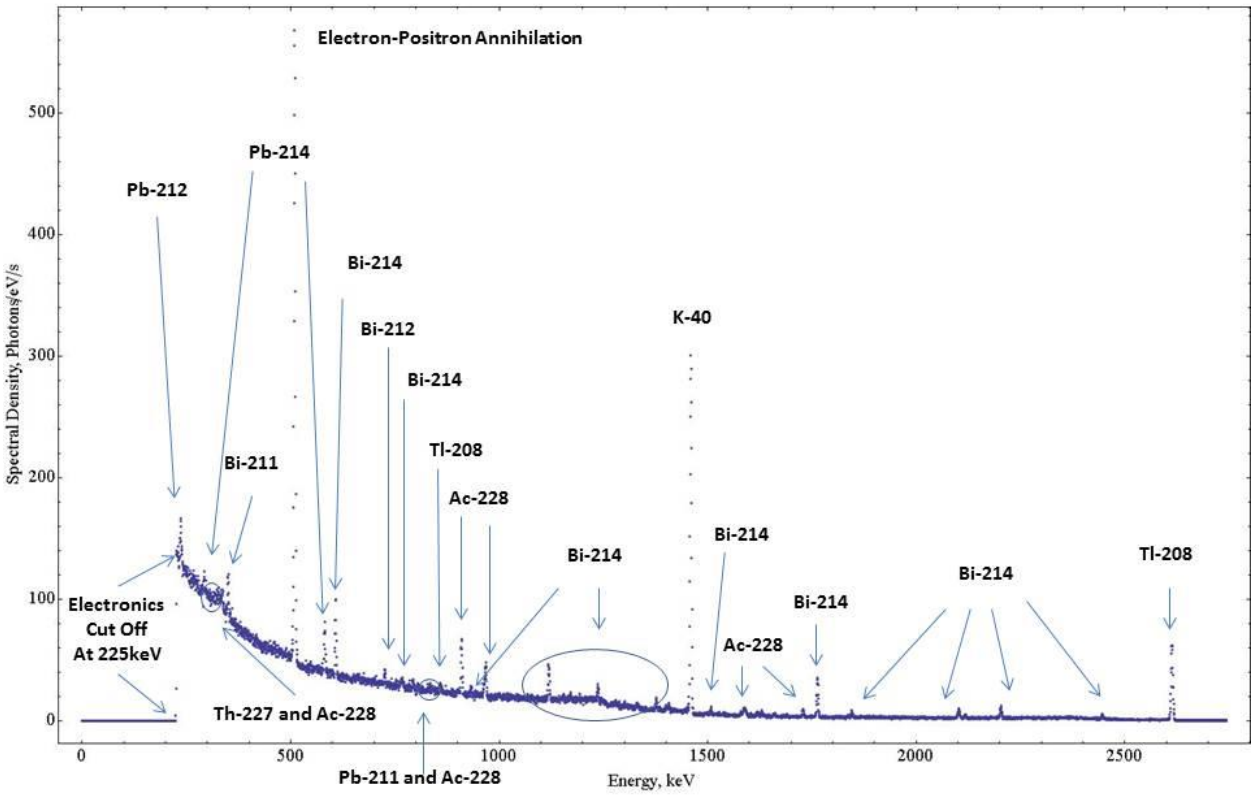

Figure 3.10. Detector 1: Background run; zoom in on the area with background peaks.

Those runs provide us with a natural counting rate for primordial isotopes around our detectors. We concentrate specifically on the K-40 line at 1.46MeV, which provides the highest count total. Background supplies count rate in this peak when there is no beam on target and thus the dead time of the detector is negligible. Production runs, and runs when the beam is on target and the experimental chamber is alight with noise, result in significant dead time. We use the reduced strength of K-40 peak during the productions runs to evaluate the dead time of the detectors during the runs. Section 2.12 describes the algorithm in detail.

Each production run took around one hour. Using dead time correction as discussed above, we meaningfully combine all experimental runs together into four final spectra: detector response at zero and 90 degrees, with and without the brick in the beam upstream.

Absolute efficiency is the probability of accurately measuring incoming gamma-rays' energy. This can be inferred from the calibration data, taking into account the fact that most scattering processes have cross-sections inversely proportional to energy. This inverse proportionality holds approximately true for energies between 1 and 10 MeV. In general, this depends on the

size and shape of the detector used. In this experiment we endeavor to test the directionality of different scattering channels at the same energy. Thus the absolute detection efficiency of the detectors is not crucial – we will compare the signals of the same detector at different angles. We have Na-22 for the calibration.

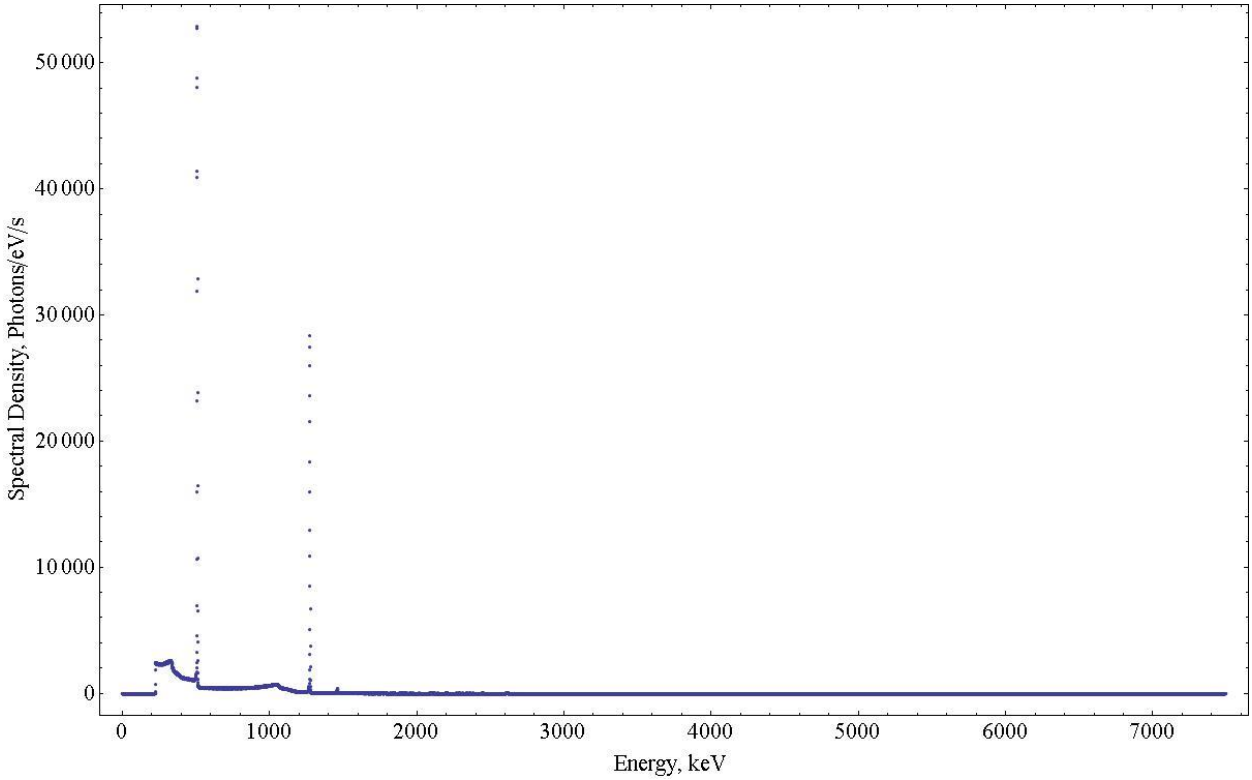

Figure 3.11. Calibration run with Na-22. The electron-positron annihilation peak and the Na-22 peak are two main peaks. The start of the Compton continuum is observable several hundred keV below the Na-22 peak.

Comparing the known activity of the calibrating source to the counting rate of the detector gives us absolute detection efficiency at the energy of the source. This ratio includes geometry, attenuation due to the shielding of the detector, and detection efficiency by the detector itself. The inverse proportionality law enables absolute efficiency calculation at the energy of interest (5.903 MeV).

Detector	1	2	3	5
Abs Efficiency	$(2.51\pm.02)*10^{-4}$	$(7.48\pm.07)*10^{-5}$	$(2.55\pm.02)*10^{-4}$	$(8.55\pm.05)*10^{-6}$

Table 3.4. Absolute detection efficiencies at 5.903 MeV.

The uncertainties are derived from the total number of counts in the calibration peaks, upper bounds on the possible positioning errors, and other geometrical considerations.

Notice that we are talking about detection efficiencies of the setup, not the detector's efficiency. Shielding and (more importantly) the solid angle subtended by the detector directly affect results in table 3.4. Detector 1 and detector 3 were practically the same distance from the target, had the same shielding, and were of the same type. This results in the almost identical efficiency of detection for those two detectors. Furthermore, detector 2 was farther away from the target. Geometry in this case dictates significantly lower efficiency. The square root of the ratio of efficiencies correlates to the ratio of target-detector distances (both are around 1.9).

Even though detector 5 is more inherently efficient (120% vs. 60% relative to the 3"x3" sodium iodide detector), it was significantly farther away (multiple meters vs. dozens of centimeters) from the target. This explains the very low efficiency of detection for detector 5.

Detector 1 and detector 3 were always at $\theta = 100$, and detector 2 was at $\theta = 150$. Our production runs alternated between $\varphi = 0$ and $\varphi = 90$. Detectors were mounted on the aluminum rig to hold them in place. Stability was of concern during this engineering task; the detector mounting rig needed to be sturdy, yet not have a lot of mass where it could scatter gammas into the detectors. Detector-foil distances were set according to our specific concerns at various scattering angles. At $\theta = 150$ we minimize the chance of beam clipping (detectors have to be at least 4 inches away from the center of the beam). At $\theta = 100$ we can't clip the beam, so the detectors were moved as close to the target as the rig would allow.

Figure 3.12. Detector holding rig installation. Detectors are rigidly mounted at $\theta = 100$ and $\theta = 150$. The whole assembly rotates between $\varphi = 0$ and $\varphi = 90$.

3.4 Experimental runs: Combining raw data into final histograms.

We had four detectors running during our production runs. Each production run results in an energy spectrum. This spectrum is normalized to account for the dead time of the detectors. Then all spectra pertaining to the same experiment are averaged. The end result is a spectrum of detected counts per hour vs. the channel number of the detector. Detectors are calibrated for energy, i.e., the known energy of background peaks yields channel number vs. energy conversion. The following are combined spectra for detector 1 for four production runs:

Run Number	φ	BRICK
1	90	Out
2	90	In
3	0	Out
4	0	In

Table 3.1. Production run parameters.

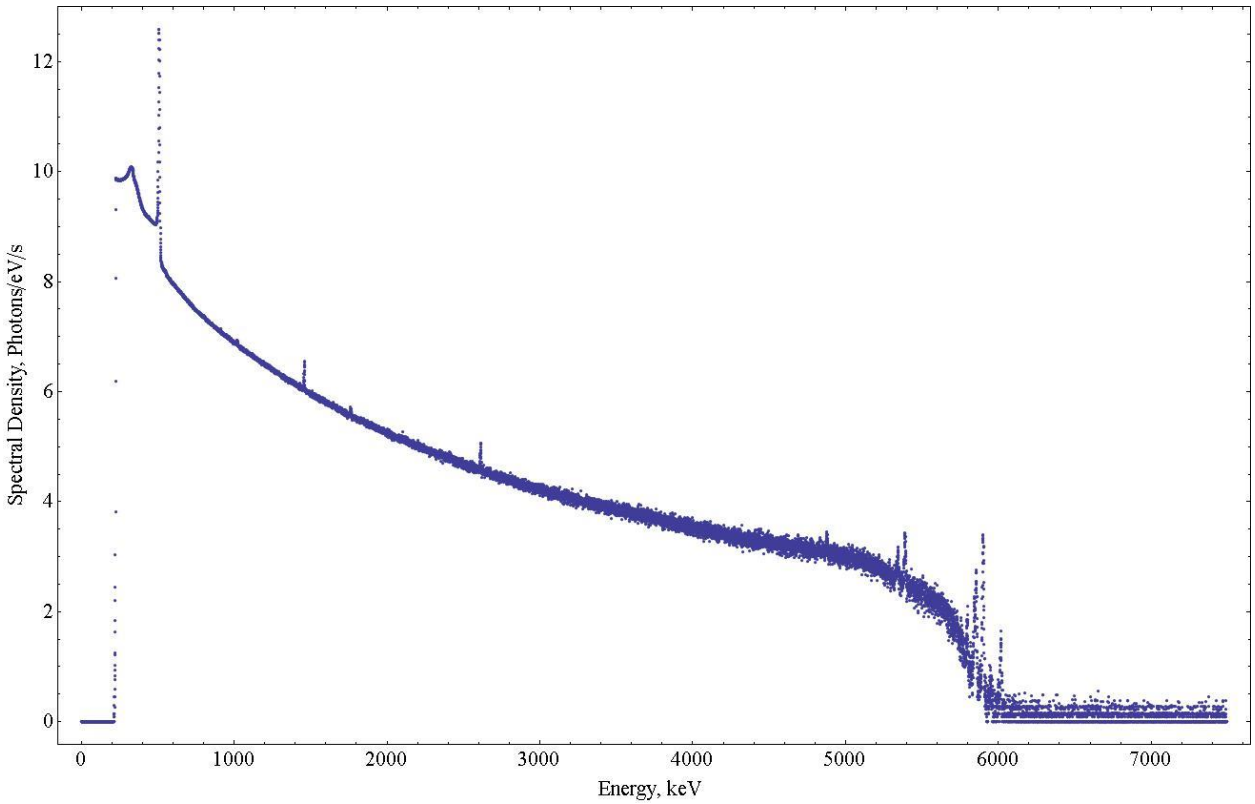

Figure 3.13. Spectrum of detector 1 run 1 (logarithm of counts per hour per detector bin vs. energy).

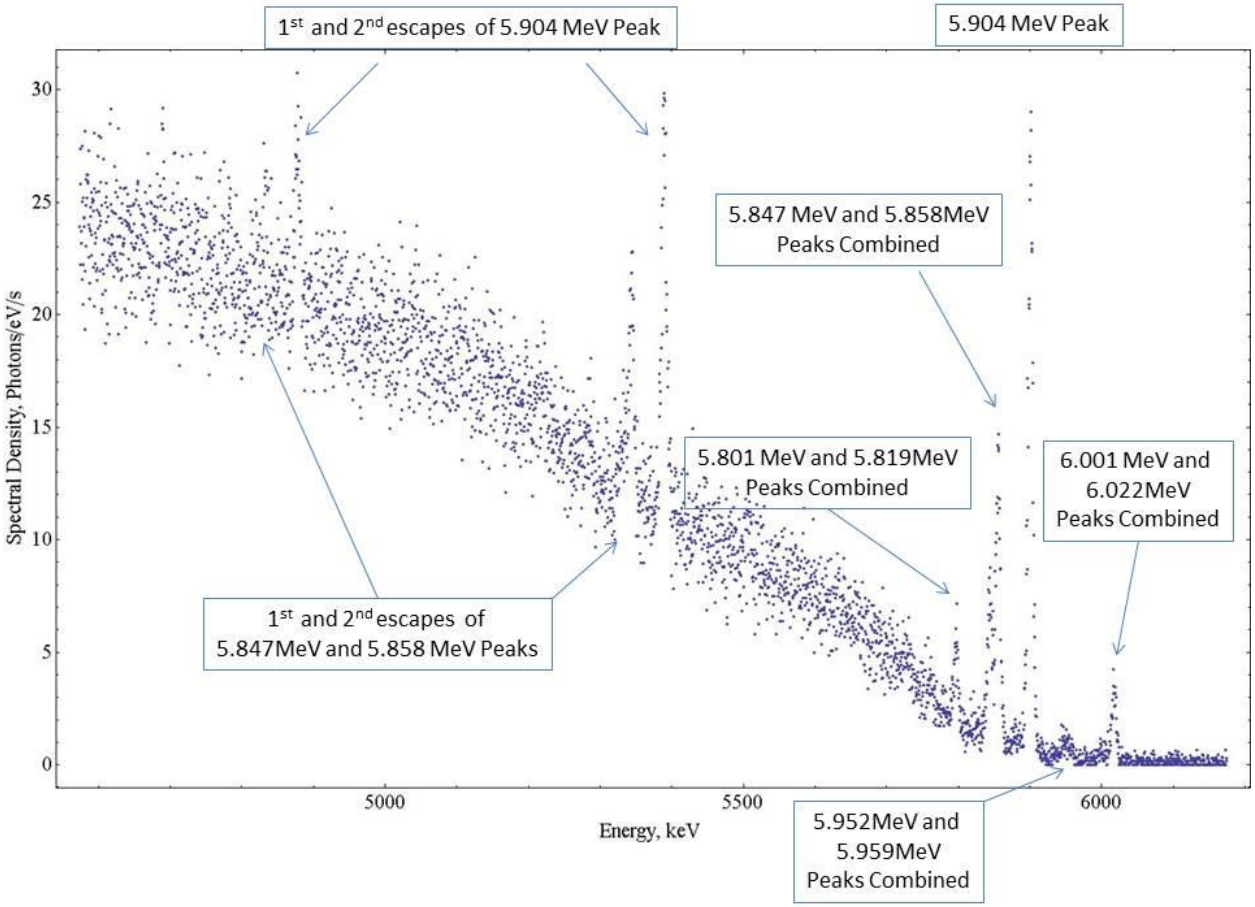

Figure 3.13a. Zoom in on the spectrum of detector 1 run 1. Some of the peaks identified (see tables 3.5 and 3.6)

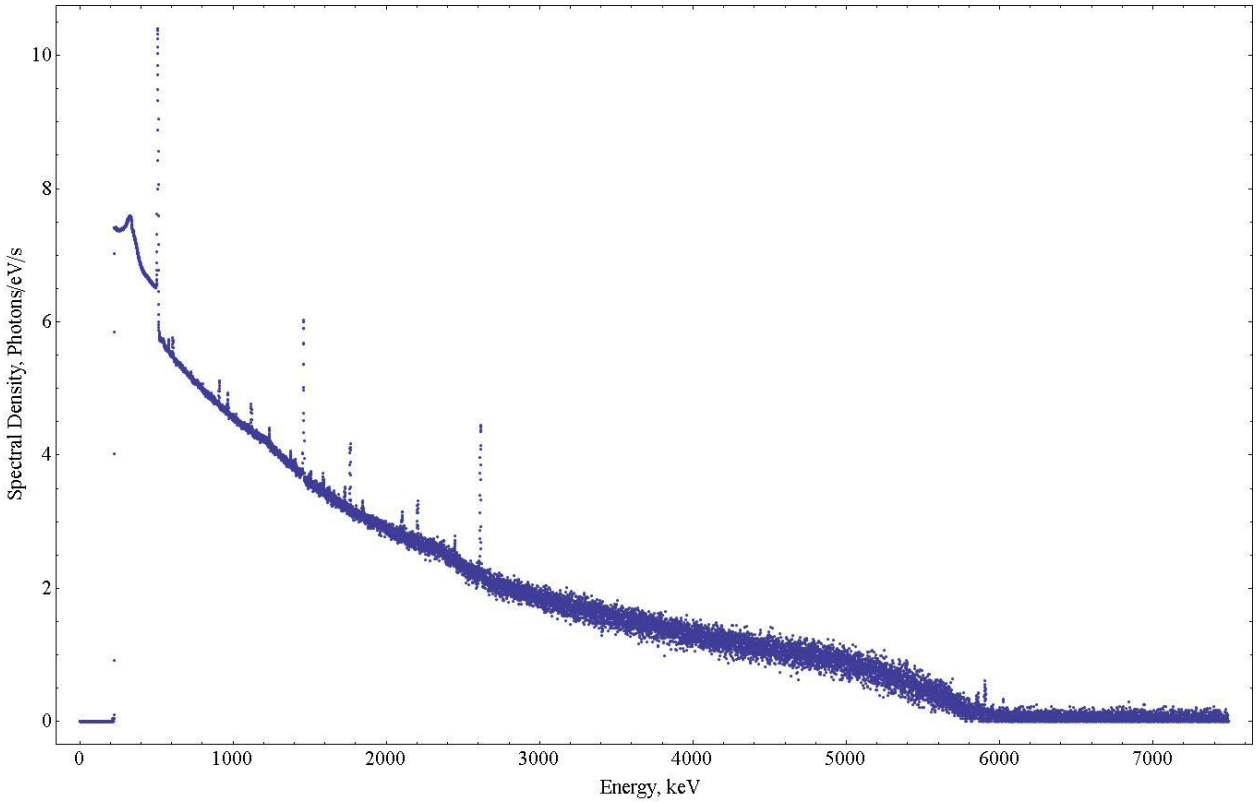

Figure 3.14. Spectrum of detector 1 run 2 (logarithm of counts per hour per detector bin vs. energy).

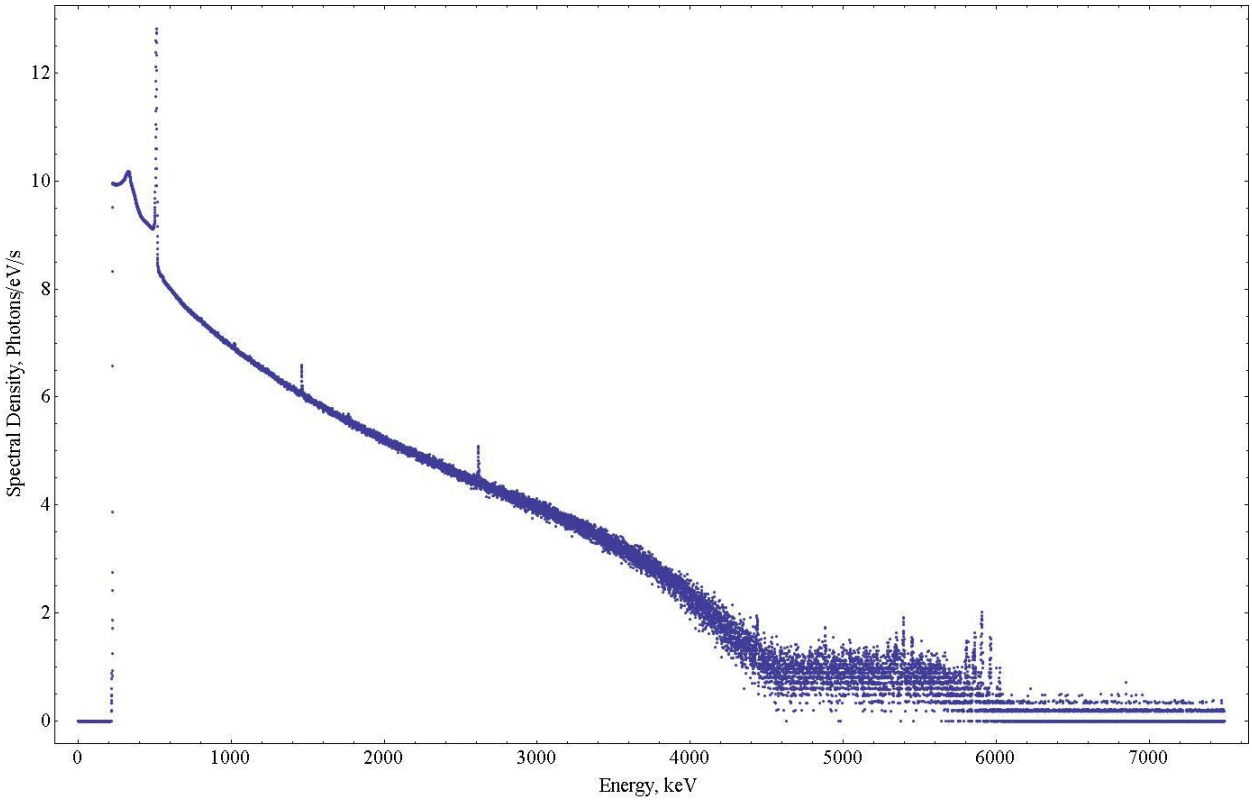

Figure 3.15. Spectrum of detector 1 run 3 (logarithm of counts per hour per detector bin vs. energy).

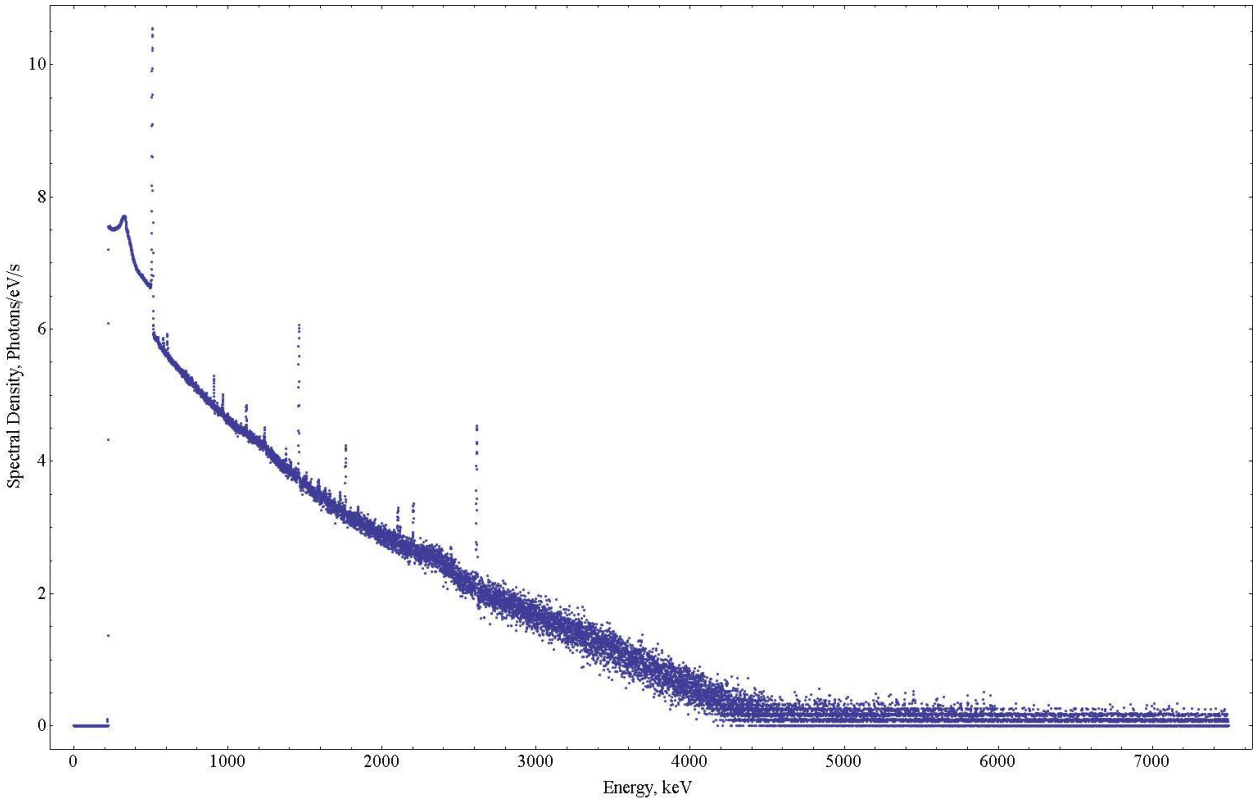

Figure 3.16. Spectrum of detector 1 run 4 (logarithm of counts per hour per detector bin vs. energy).

3.4 Nuclear resonance fluorescence (NRF) peaks detected

There are several NRF peaks spanning the bandwidth of the HIγS beam. We saw and measured some of them during some of the runs. The following table shows the peak energies (with cross sections) that we might see:

			A1	A2	B1	B2	(*)	C1	C2	D1	D2
Energy, MeV	5.733	5.762	5.801	5.819	5.847	5.858	5.904	5.952	5.959	6.001	6.022
σ, eVb	510	240	580	85	390	730	1150	42	110	29	210

Table 3.5. NRF peaks expected. Here we use the letter σ to denote integrated cross-section in eV-barns.

The column marked with an asterisk is the main line. It is so powerful that first and second escape peaks from it are observable. Furthermore, some lines are too close to each other to resolve. A1 and A2, B1 and B2, C1 and C2, and D1 and D2 are united for the data analysis. In the results table each of those pairs gets a single column.

Among many methods to estimate the strength of the peak from data, we chose two. The first approach fits a Gaussian on top of the background to the data points around the peak. The area of the Gaussian is the strength of the peak. The second approach takes the total number of the counts in the peak and subtracts background counts inferred from areas immediately above and below the energy of the peak. The inference assumes linear dependence of the background on energy—which holds true for small energy intervals (we used 20–40 channels above and below the peak, which translates to 10–20 keV). Both methods gave the same result for the main peak, proving equivalency of the methods. Addition is computationally easier than the Gaussian fit, so the second method was carried over for all of the data.

A standard deviation of the measured peak strengths was derived from the data. Variances on the number of counts in the peak, above the peak, and below the peak are equal to the numbers themselves. Those three counting windows each have their own number of channels. A standard deviation of the result is derived through standard error propagation formula (adding variances weighted by the number of channels in each counting window).

The main line is strong enough to present first and second escape peaks. Lines B1 and B2 combined are strong enough to exhibit the first escape peak. Escape peaks will not have cross-sections associated with them because the phenomenon is complicated and describing it exactly might prove to be too cumbersome.

	2nd escape from (*)	1st escape from (**)	1st escape from (*)				(**)	(*)		
Energy, MeV	4.882	Varies	5.393	5.733	5.762	5.801 5.819	5.847 5.858	5.904	5.952 5.959	6.001 6.022
σ, eVb	NA	NA	NA	510	240	665	1120	1150	152	239
Run 1	120	181	321	22	13	41	318	459	23	63
StDev	43	64	36	19	16	22	24	23	9	11
Run 2	2	0	6	0	2	2	5	9	3	2
StDev	12	17	9	5	4	6	6	4	3	4
Run 3	22	26	53	3	0	40	49	73	20	12
StDev	12	22	13	8	7	14	14	11	10	8
Run 4	0	0	1	0	2	3	2	1	3	0
StDev	4	7	4	3	3	5	5	3	4	5

Table 3.6. NRF peaks observed (detector 1). The numbers of the detected counts and their uncertainties.

The ratio of the peak strengths during run 1 and run 3 can be compared to the predicted values from theory. The following is the comparison:

	Run 1 / Run 3	Theory
5.904 MeV	6.29	33
StDev	.99	
5.847 MeV + 5.858 MeV	6.5	33
StDev	2	

Table 3.7. Peak strength ratios (detector 1). Run 3 produces significantly more photons than expected.

	2nd escape from (*)	1st escape from (**)	1st escape from (*)				(**)	(*)		
Energy, MeV	4.882	Varies	5.393	5.733	5.762	5.801 5.819	5.847 5.858	5.904	5.952 5.959	6.001 6.022
Sigma	NA	NA	NA	510	240	665	1120	1150	152	239
Run 1	38	64	101	2	6	19	101	129	12	15
StDev	12	20	14	8	7	10	13	12	5	5
Run 2	2	2	2	1	0	0	1	3	0	1
StDev	3	6	3	3	2	4	4	3	3	2
Run 3	22	37	77	2	3	20	68	92	14	12
StDev	10	18	12	7	6	9	11	10	5	5
Run 4	0	1	0	0	0	0	0	1	1	0
StDev	3	5	3	2	2	3	5	2	3	2

Table 3.8. NRF peaks observed (detector 2).

	Run 1 / Run 3	Theory
5.904 MeV	1.4	4/3
StDev	.2	
5.847 MeV + 5.858 MeV	1.5	4/3
StDev	.3	

Table 3.9. Peak strength ratios (detector 2).

	2nd escape from (*)	1st escape from (**)	1st escape from (*)				(**)	(*)		
Energy, MeV	4.882	Varies	5.393	5.733	5.762	5.801 5.819	5.847 5.858	5.904	5.952 5.959	6.001 6.022
Sigma	NA	NA	NA	510	240	665	1120	1150	152	239
Run 1	160	220	330	18	10	50	300	430	24	57
StDev	21	36	25	14	12	18	23	22	10	13
Run 2	2	5	5	0	1	2	9	7	1	2
StDev	4	8	4	3	3	5	5	4	4	5
Run 3	34	19	82	3	5	60	80	103	43	11
StDev	12	24	14	8	7	13	13	11	10	8
Run 4	1	0	0	0	1	3	3	2	2	1
StDev	4	7	4	3	3	5	4	3	4	5

Table 3.10. NRF peaks observed (detector 3).

	Run 1 / Run 3	Theory
5.904 MeV	4.2	33
StDev	.5	
5.847 MeV + 5.858 MeV	3.8	33
StDev	.7	

Table 3.11. Peak strength ratios (detector 3). Run 3 produces significantly more NRF photons than expected.

Recombining data for within the run comparisons:

	2nd escape from (*)	1st escape from (**)	1st escape from (*)				(**)	(*)		
Energy, MeV	4.882	Vary	5.393	5.733	5.762	5.801 5.819	5.847 5.858	5.904	5.952 5.959	6.001 6.022
σ, eVb	NA	NA	NA	510	240	665	1120	1150	152	239
Det 1	120	181	321	22	13	41	318	459	23	63
StDev	43	64	36	19	16	22	24	23	9	11
Det 2	38	64	101	2	6	19	101	129	12	15
StDev	12	20	14	8	7	10	13	12	5	5
Det 3	160	220	330	18	10	50	300	430	24	57
StDev	21	36	25	14	12	18	23	22	10	13

Table 3.12. NRF peaks observed, run 1.

Directionality of the NRF plays out differently between φ=0 (runs 1 and 2) and φ=90 (runs 3 and 4). In fact, the former scenario (φ=0) has no dependence on θ. Comparing the peaks from all three detectors (taking into account detection efficiency) confirms the statement:

	Detector 1 / Detector 2	Detector 1 / Detector 3
5.904 MeV	1.04	.99
StDev	.11	.11
5.847 MeV + 5.858 MeV	.92	.89
StDev	.14	.13

Table 3.13. Relative Peak Strengths for run 1. Theoretical prediction for the ratio is 1.

All other peaks prove to be unusable, as far as making statistical statements is concerned, due to excessively high noise.

	2nd escape from (*)	1st escape from (**)	1st escape from (*)				(**)	(*)		
Energy, MeV	4.882	Vary	5.393	5.733	5.762	5.801 5.819	5.847 5.858	5.904	5.952 5.959	6.001 6.022
σ, eVb	NA	NA	NA	510	240	665	1120	1150	152	239
Det 1	22	26	53	3	0	40	49	73	20	12
StDev	12	22	13	8	7	14	14	11	10	8
Det 2	22	37	77	2	3	20	68	92	14	12
StDev	10	18	12	7	6	9	11	10	5	5
Det 3	34	19	82	3	5	60	80	103	43	11
StDev	12	24	14	8	7	13	13	11	10	8

Table 3.14. NRF peaks observed: run 3.

	Detector 1 / Detector 2	Detector 3 / Detector 2
5.904 MeV	.23	.33
StDev	.04	.05
5.847 MeV + 5.858 MeV	.21	.35
StDev	.07	.08

Table 3.15. Relative Peak Strengths for run 3. Theoretical prediction for the ratio is .04.

It appears that we are detecting significantly more counts in run 3 in detectors 1 and 3 (or fewer in the detector 2). Theoretical prediction assumes a perfectly polarized HIγS beam (100% linear along one axis). Redoing the directionality computations with 90% along horizontal and 10% vertical moves the ratio to around .16—within the accuracy of detector 1 and closer to the one measured by detector 3.

3.5 Discussion of the data: directionality of NRF (signal)

The directionality of the NRF has been validated. The angular dependence formula works, with one exception: it appears to underestimate the number of NRF photons detected at minimum direction of the dipole. This breakdown can be explained by the nonlinearity of polarization of the HIγS beam. The directionality formula in Chapter 2 implies a 100% linear polarization. Thus, for the engineering formula in Chapter 4, we are forced to use 90% polarization along horizontal and axis 10% along vertical. Imperfect polarization might have various causes; the five-paddle beam intensity monitor upstream might introduce secondary scatters, or the source itself might not be perfectly polarized. It is challenging to address this directly without separate comprehensive studies.

A lead brick upstream has definitely been detected. Comparing results between runs 1 and 2 and runs 3 and 4 yields a definite result: there is significantly less NRF happening in the foil per

incident photon. (The incident photon normalization takes into account the 9% flux attenuation due to the brick upstream.)

	Peak Run 1	Adjusted Peak Run 2	Peak Run 1 / Adjusted Peak Run 2
Detector 1	459	100	4.6
Detector 2	129	33	3.9
Detector 3	430	78	5.5

Table 3.16. Same detector NRF peak ratios runs 1 and 2. Adjustment is made per incident gamma-ray on the foil.

The table shows that if we take out of consideration the attenuation introduced by the brick, we get 4 to 6 times fewer NRF counts with the brick in. The ratio numbers would have small error bars on them, because Peak 1 numbers are detected with a high level of confidence.
The fact that we see any counts during Run 2 is strong evidence toward a notch refill effect happening in the brick. The notch is created by the NRF occurring in the brick. Even though natural lead has only about 24% Lead-206, five centimeters reduces the number of NRF-capable photons in the beam by a factor of 10^{-8}. We should not be able to observe any NRF peaks during runs 4 and 2. Indeed, run 4 yields no usable peak information. Run 2, however, has detector 1 and detector 3 observing the peak within two sigma (91% confidence). This is thought to be due to the low angle Compton in the brick refilling the notch, scattering down into the NRF capable range. Awareness of notch refill is essential for the design presented in Chapter 4.

Comparing the counts of the main peak with counts in secondary peaks allows for a check on the bandwidth of the beam. We take the ratio of the main peak to combined 5.847 and 5.858 peaks, normalize it by the ratio of the cross-sections, and multiply it by Gaussian factor (200keV FWHM, or σ= 85 keV) to arrive at 1.18, 1.05, and 1.17 for detectors 1, 2, and 3 respectively. The number should be 1 in a perfect world. The individual numbers have a standard deviation of about 5%, so we have mildly encouraging agreement.

3.6 Directionality of the coherent scattering: the noise

Let's consider how the data should look if we remove the bins containing the NRF counts. With an ideal detector one would see a clean Gaussian following the spectrum of the incident beam. Real detectors have numerous secondary effects, one of which is called the Compton continuum. A sharp peak (such as an NRF peak) will have a structure several hundred keV below the main peak. This structure is created by all photons of the peak that undergo single Compton scattering in the detection medium. Those photons escape the detection medium after the scattering. Thus the detector sees only energy deposited in this single scattering. A maximum energy of Compton continuum is thus the maximum energy that can be transferred to an electron during classical Compton scattering. Multiple Compton scattering can also contribute to this part of the spectrum.

In our setup, the highest significant peak is around 6.022 MeV; the Compton continuum for this peak should start around 5.777 MeV. In our setup we did not have adequate statistics to see the nice Gaussian, because the cross section for elastic non-NRF scattering is very small. However, we can still integrate all elastic counts between the main 5.904 MeV peak and the next peak above. Detector 2 provided very low counts, yielding huge uncertainties, because backwards Compton scattering is almost impossible compared to 90 degree scattering.

	Run 1 / Run 3	Theory
Detector 1	2.33	1
Detector 2	11.5	4
Detector 3	2.34	1

Table 3.17. Run 1 vs. run 3 for elastic scattering.

The discrepancy here is due to the interaction between detectors and the backgrounds in the cave. We have rotated our rig between runs 1 and 3. This means that we would have altered the detector response function, causing secondary and tertiary scatterings to find their way into detectors.

Taking ratios Detector 1/Detector 2 and Detector 3/Detector 2 (same φ, different θ) gives better results:

	Det 1 / Det 2	Det 3 / Det 2	Theory
Run 1	3.33	4.78	3.76
Run 3	16.5	23.6	14.6

Table 3.18. Same run, different detectors. One can observe somewhat encouraging agreement between theory and experiment.

3.7 Experiment conclusion: validation of the formulas for the signal and the noise

For NRF: Experimental data presented here validates our directionality models. Slight nonlinearity in polarization (~10%) of the HIγS beam might explain the abnormally high NRF counts in NRF-poor direction. Multiple crosschecks point to the validity and self-consistency of the measurements.

We have definitely detected lead upstream. Table 3.16 illustrates the attenuation of the NRF peak. Comparing spectral response adjusted per particle incident on the foil still gives a statistically significant difference between brick in and brick out runs.

Elastic scattering has been measured to somewhat correlate to the theoretical formulas. High levels of noise relative to the low levels of signal make validation not as robust as the one for

NRF. Nevertheless, the models are well understood, and disagreements point to the experimental challenges rather than modeling deficiency.

In short:

- NRF angular dependence has been validated in this chapter (signal vs. angles).
- Elastic scattering dependence has been somewhat validated in this chapter (noise vs. angles).
- Inelastic scattering dependence has been presented in Chapter 2 (noise vs. angles).

The engineering design will build on signal vs. noise ratios at all angles.

Chapter 4. Engineering design for assay of the material of interest

In this chapter, we combine models from Chapter 2 with measurements in Chapter 3 to come up with a design for a detector. Said detector will be optimized for scan time. User-defined false positive and false negative rates will inform the setup and configuration. A discussion of the future measurements and proof-of principle experiments concludes the chapter.

4.1 Scattering from the foil: angular gamma-ray spectra and angular power spectra

HIγS beam parameters (Table 2.1) are assumed for the beam in our calculations. Taking the beam and applying attenuation of the brick, we should obtain the spectrum incident on the scattering foil. Here are the spectra transmitted through the brick for various thicknesses of the brick.

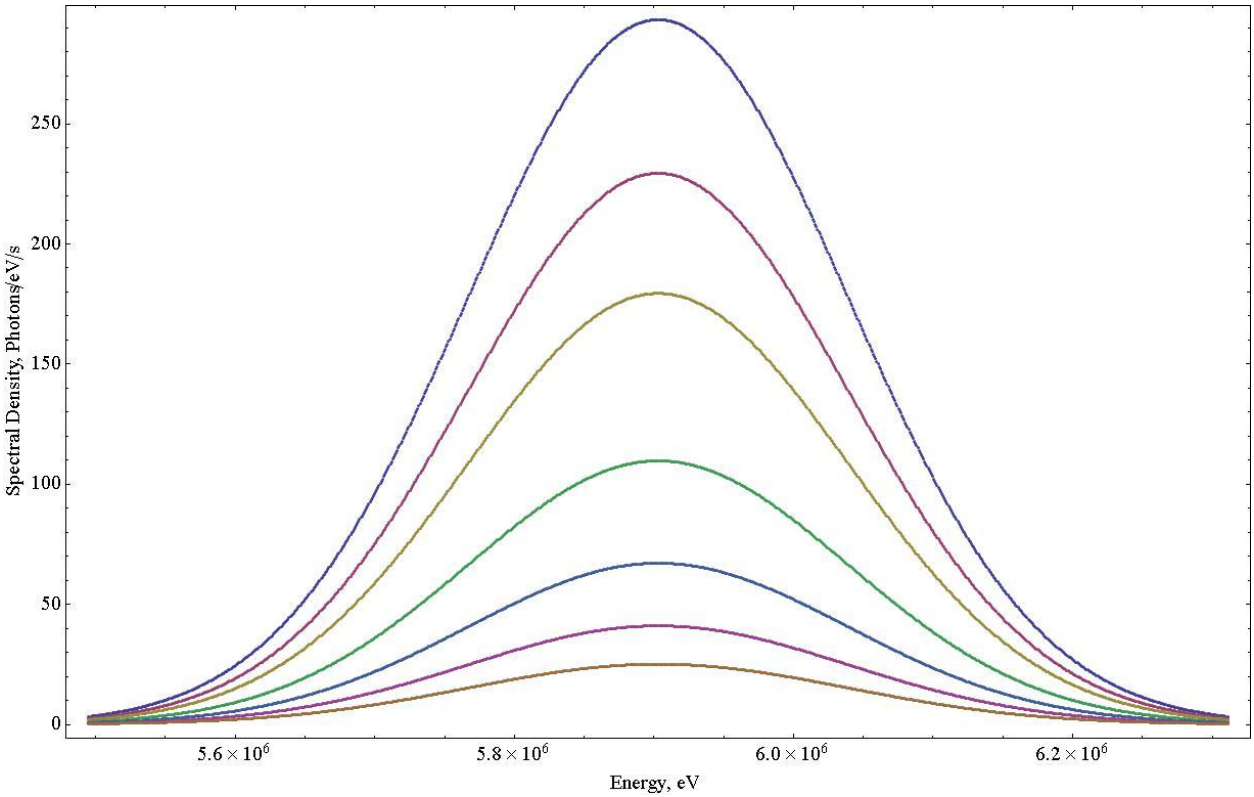

Figure 4.1. Beam incident on the foil for various thicknesses of the brick.

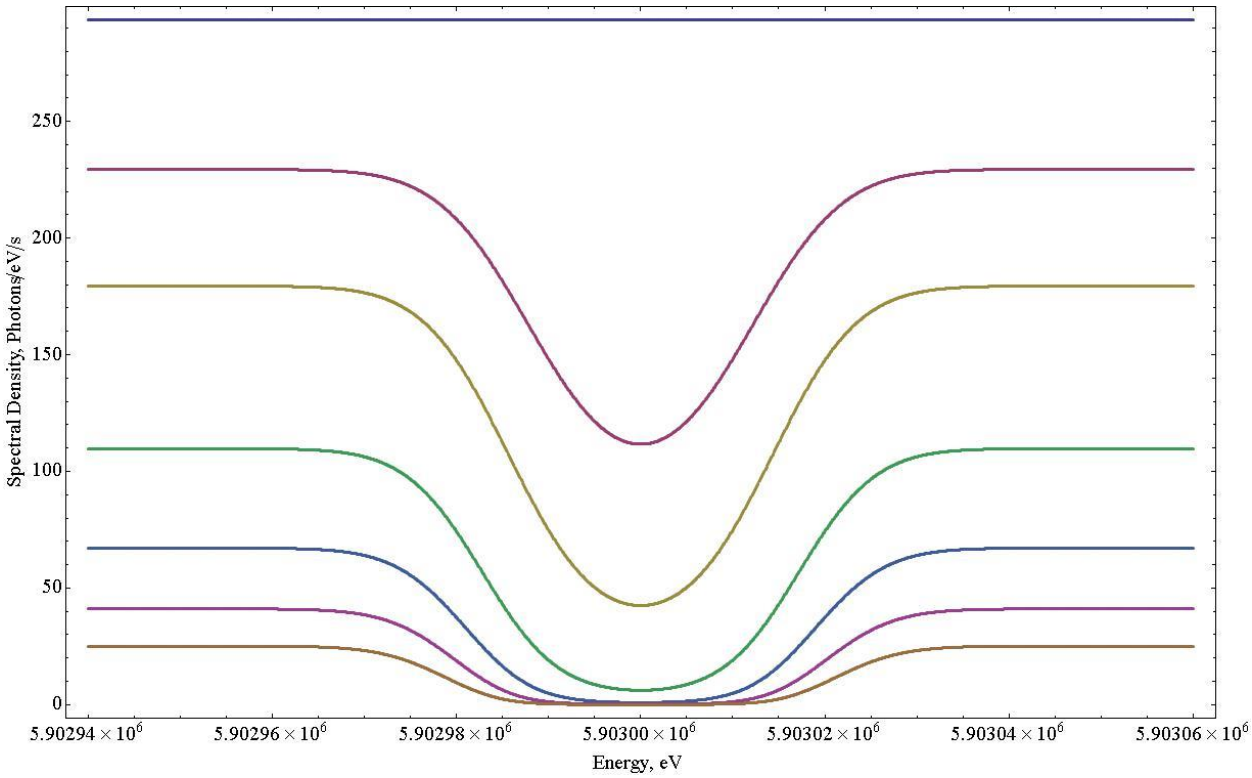

Figure 4.2. Zoom-in on the notch-area of the spectrum where NRF depleted the spectrum.

A simple scattering scenario assumes a thin foil. This assumption enables us to ignore the beam degradation as it moves through the foil on the way to and from the point of scattering being described. Here are angular distributions (photons per second vs. θ and φ) of all scattering processes described in Chapter 2: NRF (Formula 2.10), incoherent (2.17), and coherent (2.18 and 2.19). The pictures are integrals over all energies of the beam, multiplied by scattering probability in the foil.

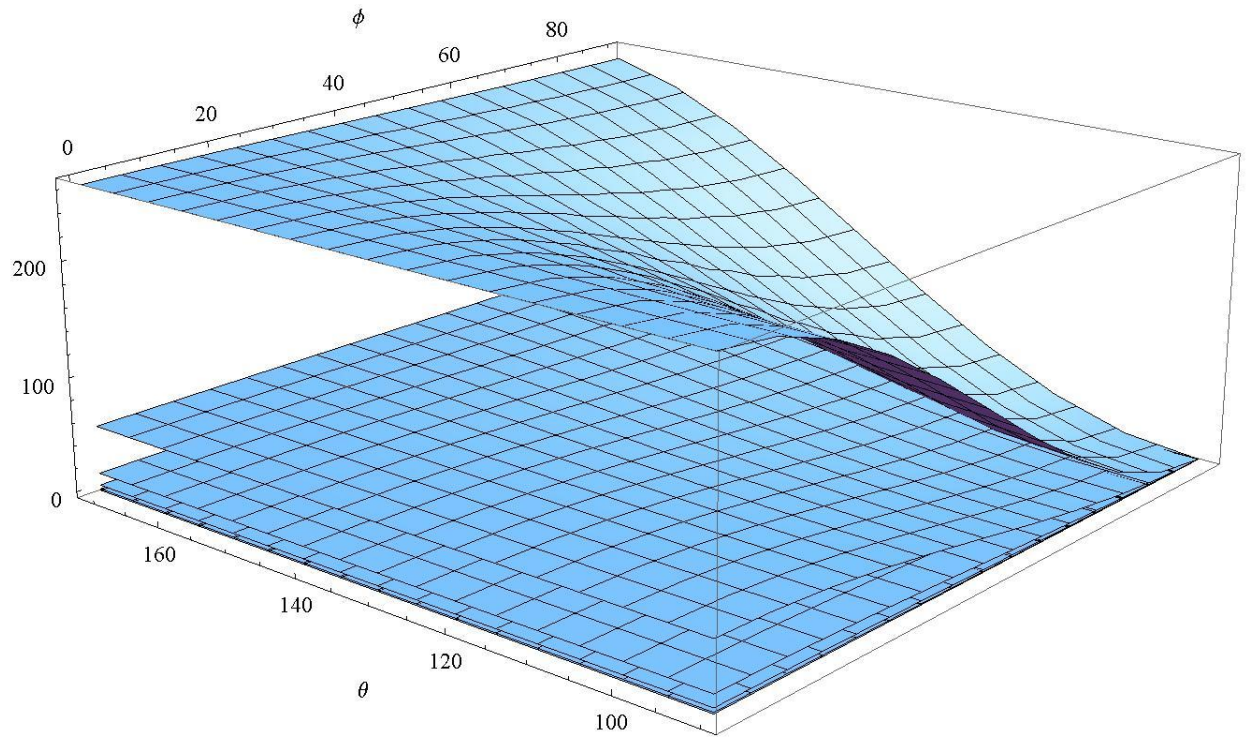

Figure 4.3. NRF angular distribution: a perfect dipole. Number of photons vs (θ,φ).

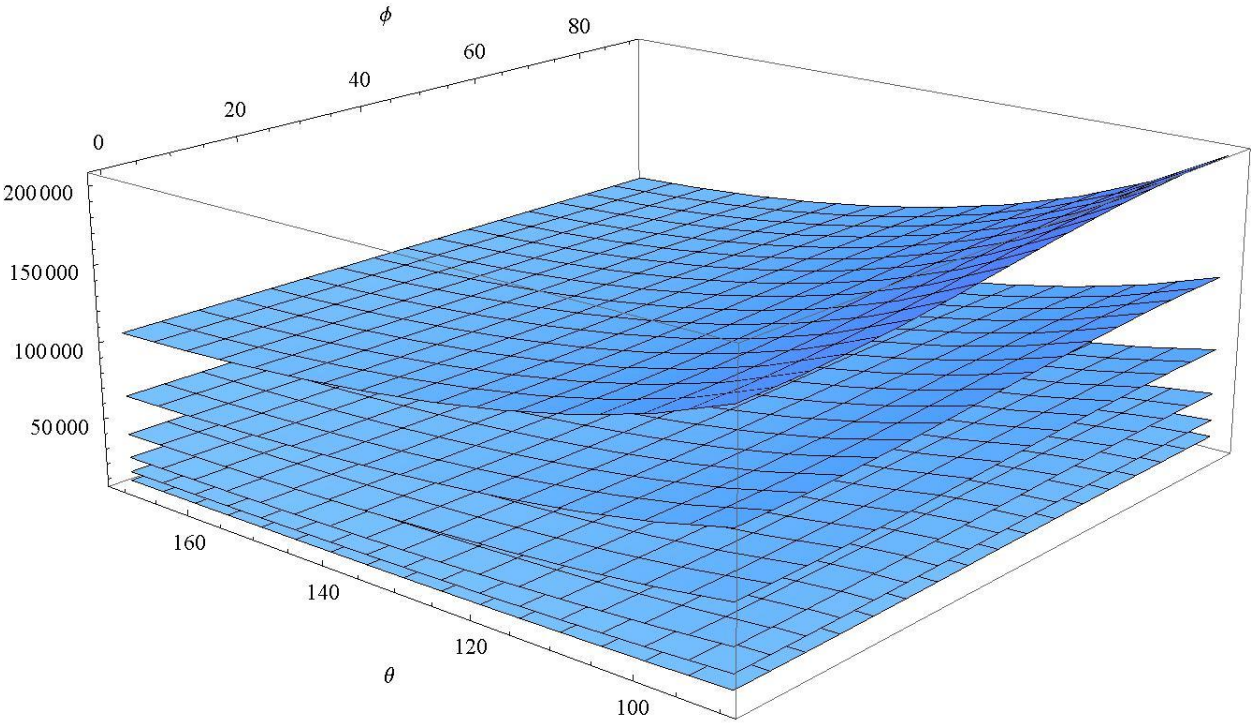

Figure 4.4. Incoherent angular distribution: main source of noise. Number of photons vs (θ,φ).

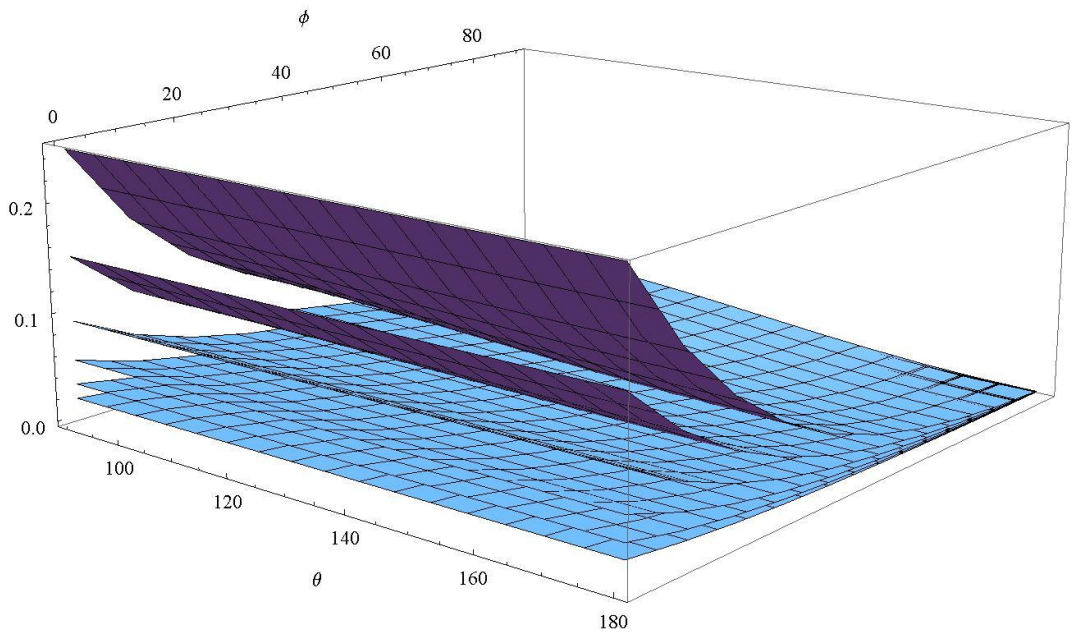

Figure 4.5. Coherent scattering: insignificant at HIγS bandwidth. Number of photons vs (θ,φ).

A more sophisticated scattering scenario assumes bulk foil. The effect of that is included in the formulas 2.26a and 2.26b. Formula 2.26a describes NRF scattering, and 2.26b describes non-NRF scattering.

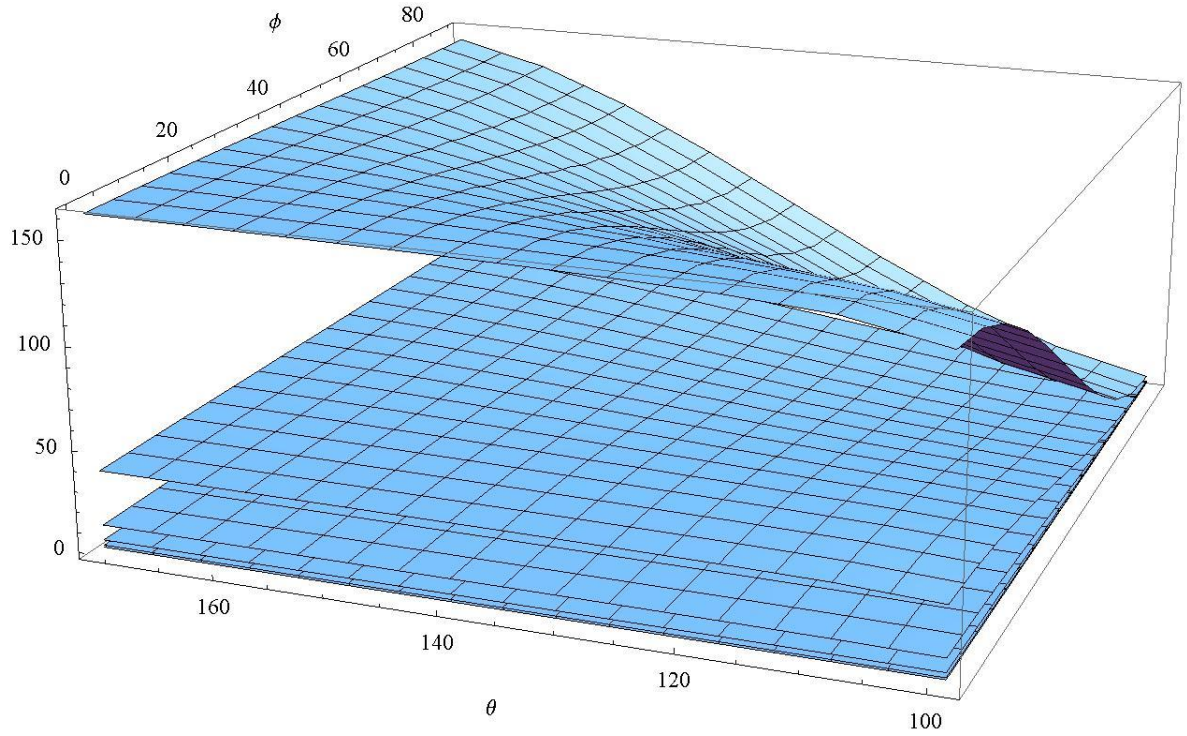

Figure 4.6. NRF angular distribution: visible is a downward curve around 90 degrees θ. Number of photons vs (θ,φ). This is due to the attenuation of the outgoing beam inside the foil.

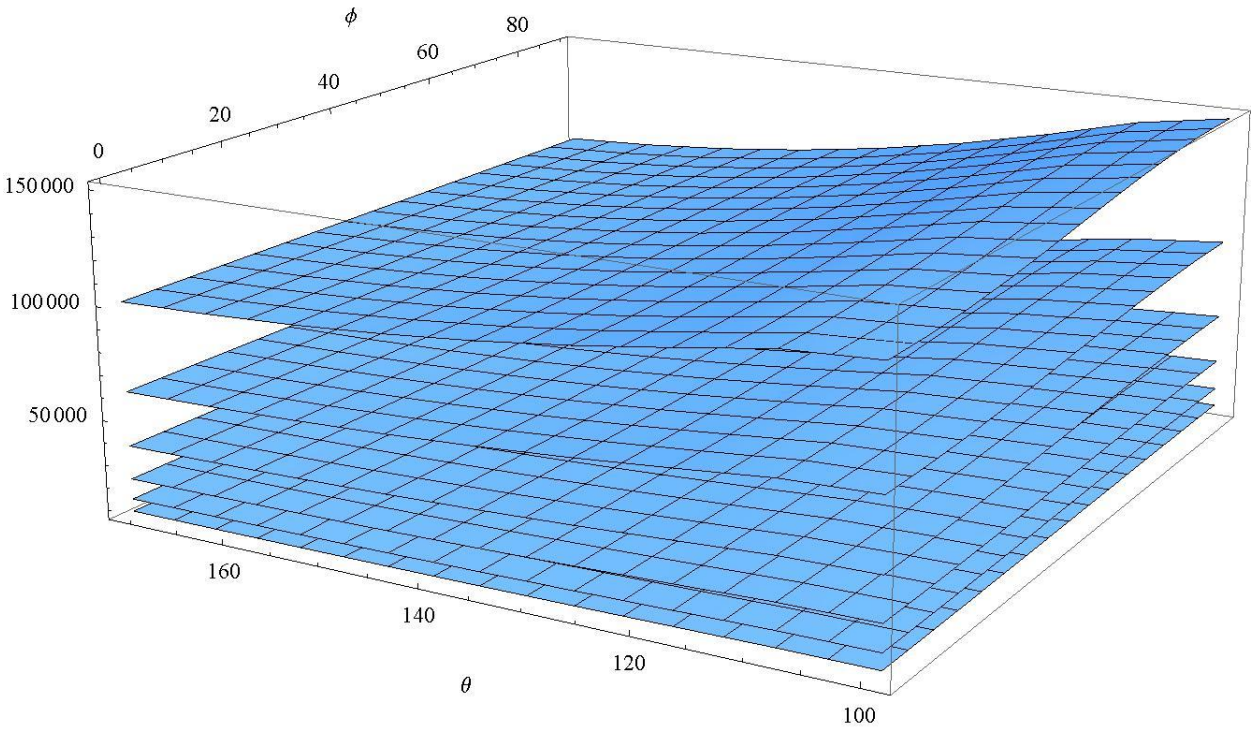

Figure 4.7. Incoherent angular distribution. Number of photons vs (θ,φ).

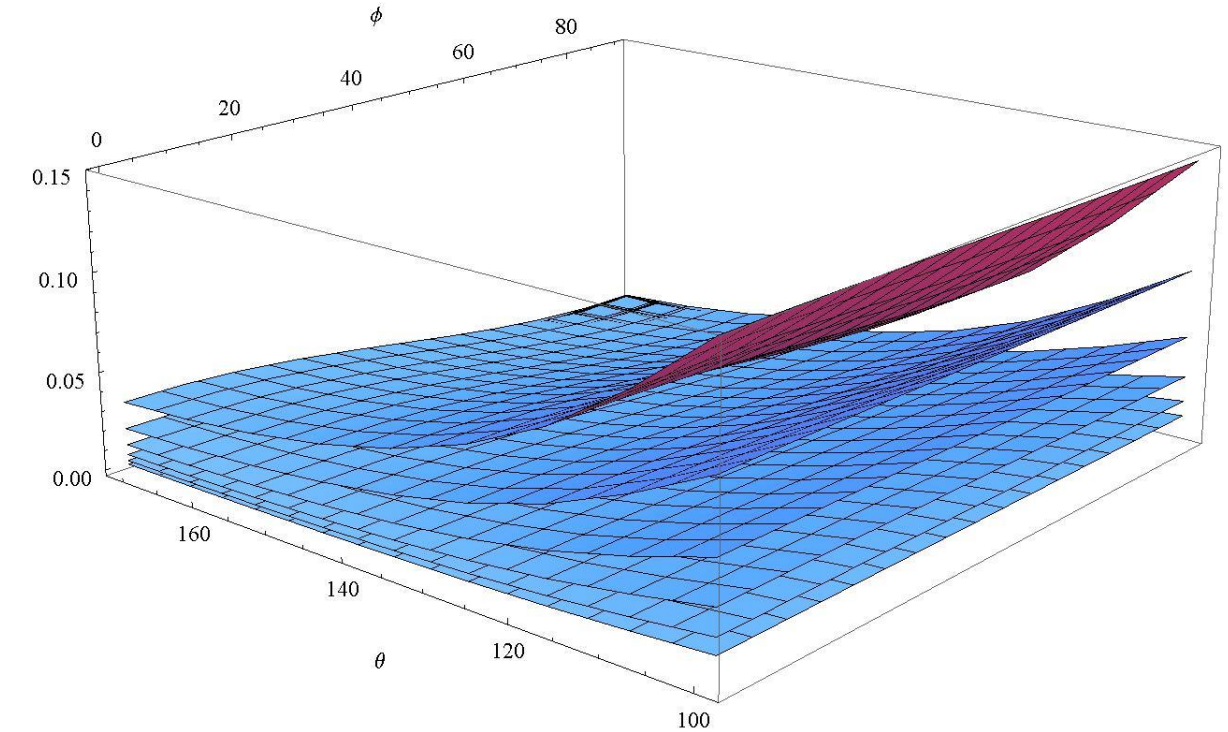

Figure 4.8. Coherent scattering. Number of photons vs (θ,φ).

Notice the depression of all signals as scattering angle θ approaches 90. Indeed, the longer the beam spends in the scattering foil, the more degraded the signal will become. If one wants to consider a 90 degrees direction, it is clear that the scattered photon needs to traverse across all the foil to get out. The radius of the scattering foil needs to be bigger than the radius of the incoming beam in order to maximize the flux on the target. One way for the forward optimization with higher-flux beams is to reduce the size of the foil to mitigate the effect.

Everything up to this point has been about single photon counting. The development of the compton based gamma-ray sources is increasing the flux to the point where other techniques are required. Higher flux means higher dead times and more experimental challenges if one is to continue to work in the single photons counting regime. Thus we introduce the current mode detection as one of the thrusts of this work – it scales up with the flux.

The current mode of photon detection measures the total energy deposited, not the total number of photons. Multiplying formulas 2.26a and 2.26b by the energy of the outgoing photon should give the energy distribution of the scattered radiation. Let us also include 3mm Cu and 3mm Pb shielding to preferentially suppress low-energy Compton scattering. The next set of figures represents the total power (eV per second) into our detecting medium vs. angle for all three processes.

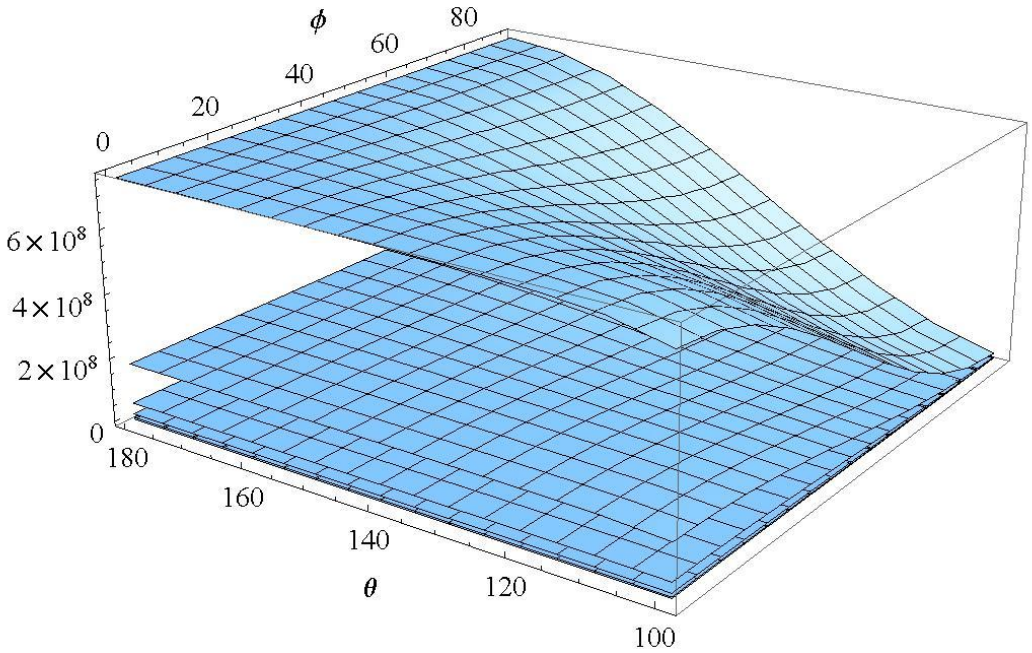

Figure 4.9. Power into the detecting medium for NRF angular distribution, eV per second.

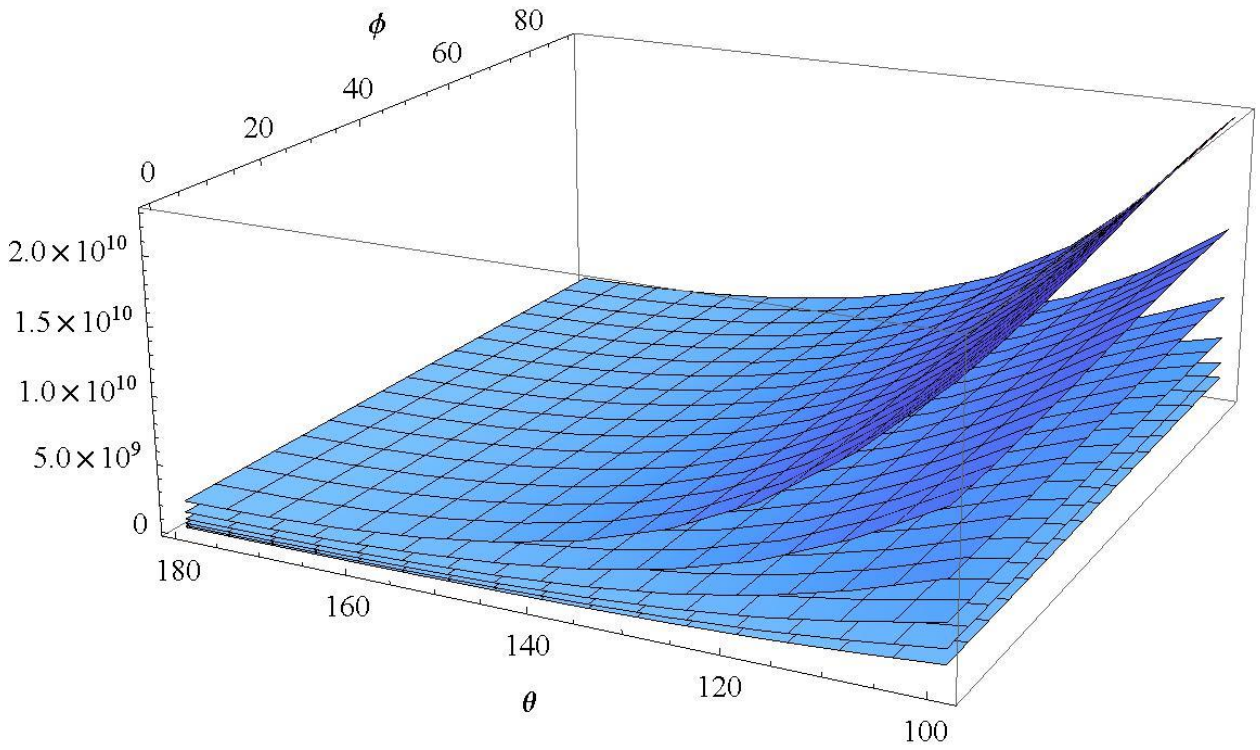

Figure 4.10. Power into the detecting medium for incoherent angular distribution, eV per second.

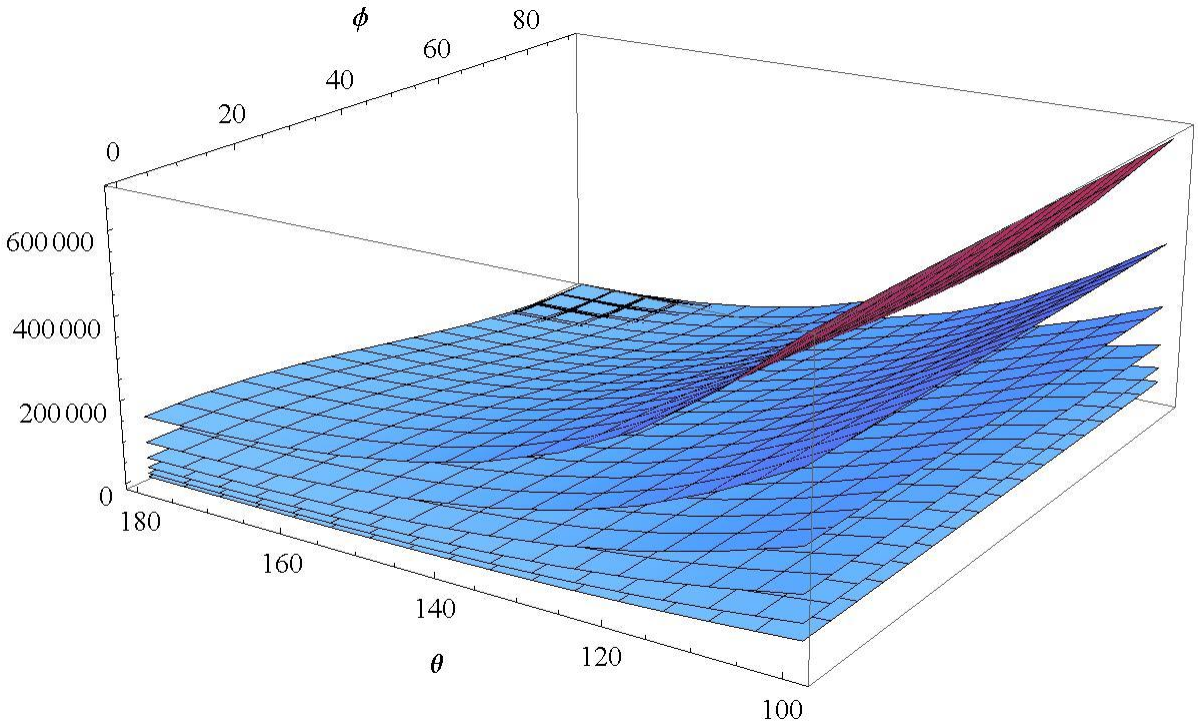

Figure 4.11. Power into the detecting medium for Coherent scattering, eV per second.

Combining all three together gives us the power vs. angle as scattered by the foil for different thicknesses of the brick.

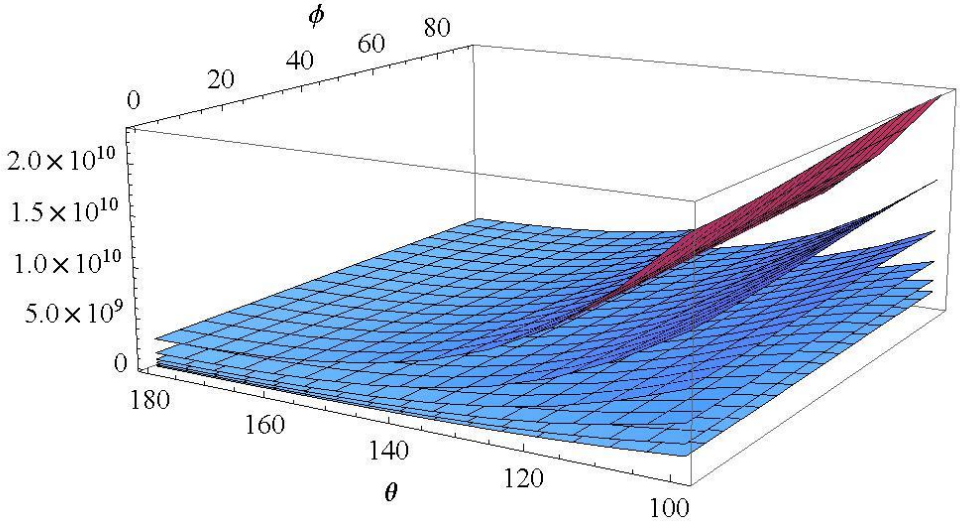

Figure 4.12. Power (eV per s) into the detecting medium vs. angle.

4.2 Detecting the power: current mode of photon detection with the scintillator

The plastic scintillator converts the gamma-ray into visible light photons. This conversion happens at the rate of a single blue photon for every ε=30eV of the gamma-ray's energy. The number of blue photons (N) created is governed by the following formula:

$$N_{blue} = E * \frac{1}{\varepsilon} \quad (4.1)$$

Where E is energy of the gamma-ray absorbed. Next, one takes into account QE—the quantum efficiency of blue photon collection. This number should be measured experimentally because it depends on scintillator geometry, particulars of blue light collection, and diode-based measurement. Integrating 4.1 over all energies gives the rate of detection vs. θ and φ per unit time:

$$\frac{dN_{blue}}{dt} = \int_0^\infty QE * E * \frac{1}{\varepsilon} * \frac{dN_{in}}{dEdt} dE \quad (4.2)$$

Where N_{in} represents the spectral density of incoming gamma-rays. This rate is in number of blue gammas detected. The connection with total power into the scintillator becomes apparent when we pull the constants out:

$$\frac{dN_{blue}}{dt} = \int_0^\infty QE * E * \frac{1}{\varepsilon} * \frac{dN_{in}}{dEdt} dE = \frac{F*QE}{\varepsilon} \int_0^\infty E \frac{dN_{in}}{dEdt} dE = \frac{QE}{\varepsilon} * P_{in} \quad (4.3)$$

Assuming the QE of respectable 0.1, one gets (if we are careful to keep our power in eV):

$$\frac{dN_{blue}}{dt} = 0.0033 * P_{in}$$
(4.4)

Equation 4.4 connects the power distribution presented in Figure 4.12 to the total number of photons counted by the electronics at the output. Our uncertainty thus becomes:

$$\sigma_{signal} = \sqrt{N_{blue}} = \sqrt{0.0033 P_{in} * t}$$
(4.5)

All the formulas in this section refer to quantities that depend on θ and φ—those dependencies have been ignored for clarity. The next section will see reintroduction of angular dependence.

4.3 Inferring the amount of NRF from the measured data

Our challenge thus becomes to look at 4.12 received from the measurement, and extract 4.9 to make the determination. We propose to use a reference direction of no NRF (θ =90 φ =90) to measure coherent and incoherent scatterings at this direction. This is used to define coherent and incoherent for any angle because directionality of those radiations is deterministically defined (Fig 4.11 and 4.10).

Thus the procedure is as follows:

- Measure raw data at various directions (points on 4.12).
- Use reference direction (90, 90) to infer coherent (4.11) and incoherent (4.10).
- Subtract coherent and incoherent contributions from data; we retrieve the total signal attributable to NRF this way.
- Analyze the resultant NRF contribution.

Our signal and uncertainty are thus (applying 4.4 to the difference and integrating over time):

$$N(\theta,\varphi) = 0.03 * \ P_{NRF}(\theta,\varphi) * time$$
$$\sigma_N^2(\theta,\varphi) = \sigma_{P_{tot}}^2(\theta,\varphi) + \sigma_{P_{tot}}^2(90{,}90) = 0.03 * \left(P_{tot}(\theta,\varphi) + P_{tot}(90{,}90)\right) * time \qquad (4.6)$$

4.4 Using the detector: user inputs determine the integration times

Considering the detection scenario one needs to have two quantities defined by the user: the threshold amount of material and the confidence of the detection. The threshold amount multiplied by the density and divided by the cross-section of the beam would give us the thickness of the material that we are endeavoring to detect. This would enable us to choose the correct surface from the family of curves graphed above. User specifies confidence level for the detection. Statistics gives us the threshold z score from the confidence level — one can look it up in tabulated bell-shape curve integral. This score needs to be surpassed by z score from the measurement for the detection:

$$Z = \frac{P_{measured} - P_{expected}}{\sigma_{measured}} \qquad (4.7)$$

Equation 4.6 gives the standard deviation and equation behind figure 4.12 gives the expected value. If the z score measured surpasses threshold z score we detect the material. Otherwise we claim there is no material of interest.

The challenge in the assay scenario is to determine which surface of Figure 4.9 we belong to. The user defines the desired accuracy on the amount of material assayed (which feeds into the distance between the curves). Furthermore, the user defines the confidence level of the measurement. This determines the statistical z score that one needs to achieve with the data.

From the z score and our estimates of signal (Fig. 4.9) vs. uncertainty (Fig. 4.13), the time of the integration follows.

Both scenarios have the ratio of signal to uncertainty compared to the z score from the confidence level. The signal grows linearly with the time of integration. Uncertainty grows as the square root of the time. This ensures unambiguous time determination for any detection or assay scenario.

Another way to think about this is in term of photons on the foil. All pictures above are created for a total flux of 10^8 photons per second. This number was picked to approximate the HIγS beam parameters. Total flux directly trades off with total time—all that our detection/assaying device cares about is the total integrated number of photons through the system.

4.5 Detector design

Taking the signal-to-uncertainty ratio and plotting it gives us an idea where to put the second scintillator. From formula 4.6, and assuming a 4 sigma requirement from the user, we get:

$$\frac{0.03 * P_{NRF}(\theta,\varphi) * time}{\sqrt{0.03 * \left(P_{tot}(\theta,\varphi) + P_{tot}(90,90)\right) * time}} = 4 \tag{4.8}$$

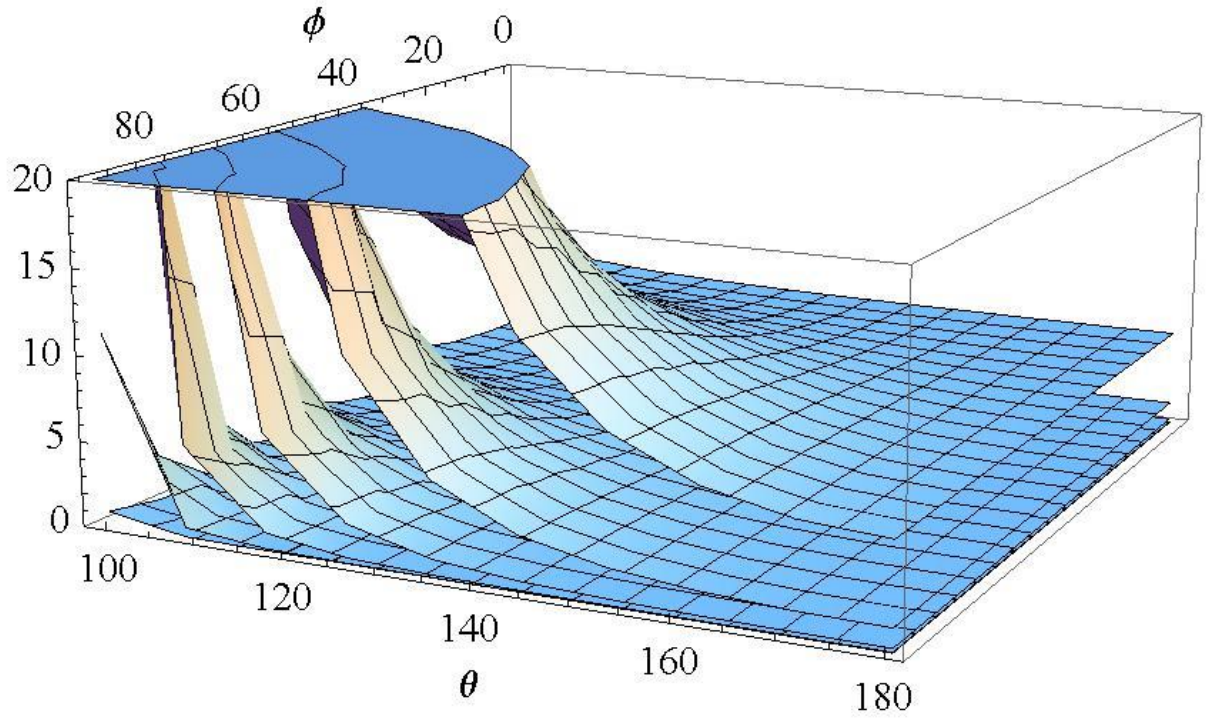

Figure 4.13. Time of integration vs. angle of detection unit for a 4 sigma assay.

The z axis on the figure represents the number of seconds one needs for the unambiguous assay. This scenario assumes flux of 10^8 gammas per second on the target at the bandwidth of around 100 keV. Thus we are requiring the fluence on the order of total 10^8 — 10^9 gammas for the assay to be successful.

One can observe how detection time explodes when we get closer to the reference direction (in the figure above this vertical asymptote is outside of the zoom). Indeed, moving towards reference direction reduces signal and increases noise. In the limit when detection unit and reference unit are on top of each other the integration time is infinite. Signal (inferred from difference between detection unit and reference unit) goes to zero while noise remains steady.

Of course, Figure 4.13 represents the ideal response of the detection system -reality is never as compliant as theoretical models make it out to be. Degradation of the scintillators, electronics-induced inaccuracies would definitely interfere with the operation of the detector.

It appears that we need to be as far back as possible. Indeed, the main contributor to the noise dies off as the scattering angle get closer to 180 degrees. The signal, on the other hand, peaks at total backscatter. It is not practical to consider back angles larger than 170 degrees because we need to leave enough space for the beam to enter the detector setup. Thus we choose 170 degrees for our θ. Formula 4.7 gives the integration time needed for a 4-sigma assay.

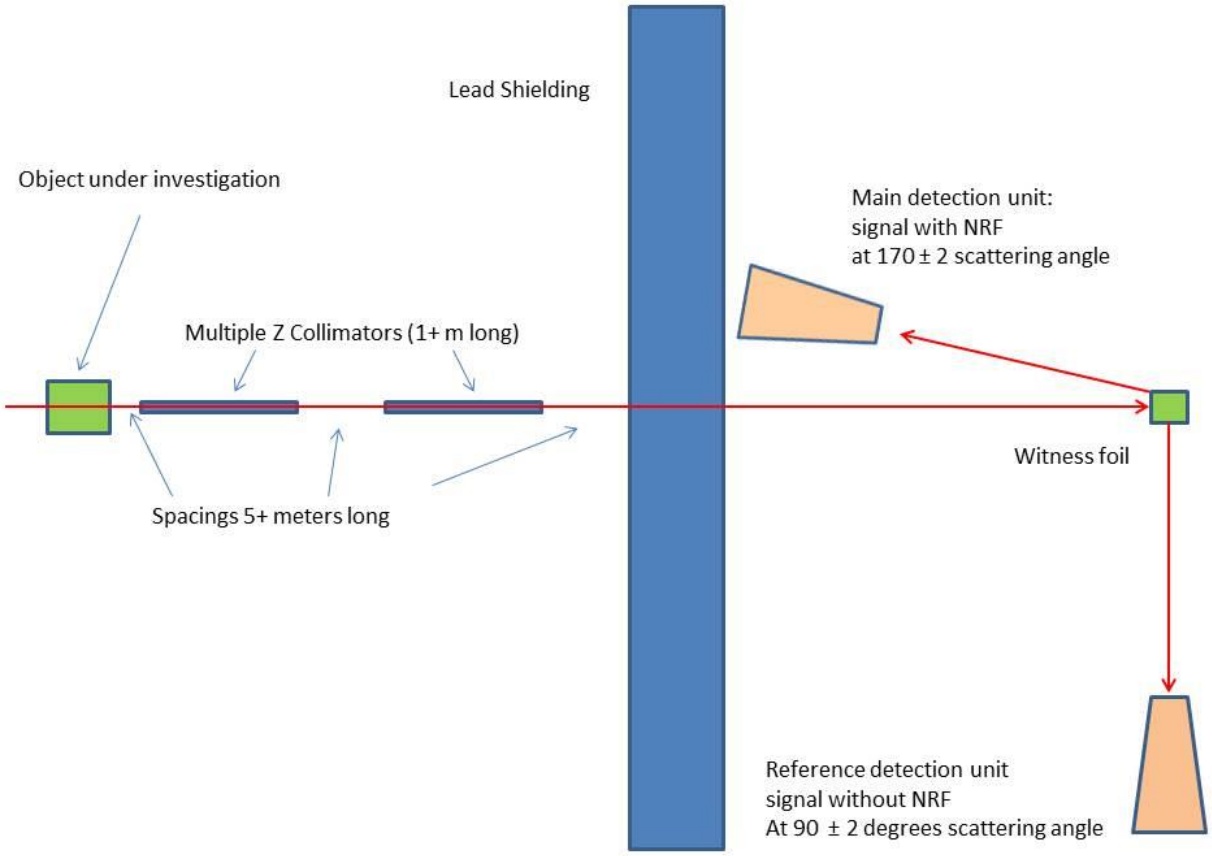

Figure 4.14. The detector system: object under investigation, spacings, collimators, shielding, witness foil, detection units.

The **Object under investigation** has to be held in place by low Z supports that do not have any resonances around the peak that we are looking for. This would ensure that minimal noise is introduced.

The object under investigation will de-collimate the beam. Furthermore, low-angle Compton scattering refills the notch, thus degrading our performance. We need a lot of **space** between the object and the collimators and shielding. This will allow all photons that underwent low-angle Compton scatterings to fly away.

Collimators are further necessary to scrape off the photons that are not along the main axis of the beam. Standard multiple Z assemblies of sufficient length are required. Lower Z inside of higher Z concentric tubes ensure gammas that are being scraped off have a very low probability of contributing to the noise.

The **shielding** is lead. We need to separate the beam preparation area from the detection area.

The **witness foil** has to be of optimal dimensions: the cross-section of the beam has to match the foil. Furthermore, it needs to be thick enough to ensure adequate representation of NRF gammas in the scattered spectrum. The witness foil holder has to be low Z and as light as possible with no NRF peaks of its own.

Detection units are shielded on all sides to cut down the background. Cu Pb shields need to be in front of them to preferentially scatter low-energy gammas. Plastic scintillators and pickup electronics get the signal and transmit it out of the detection chamber.

During the operation, the detection chamber has to be isolated; radiation has to be contained.

The rates we are expecting are represented in Figures 4.6, 4.7, and 4.8. Those spectra are number of photons per srad per eV for 10^8 photons per second as the flux on the target. These numbers could be practically detected in a single photon counting regime. Progress in gamma-ray sources will require engineering designs that would work for significantly higher fluxes.

This work considers current-mode detection for two reasons. First, the improvement of the gamma-ray sources will increase the flux on target. This will present an additional challenge, as it will drive up the dead time of the detector. The current-mode approach directly scales up with the increase of the flux. Second, the current mode weights detected photons by their energies. The noise mainly comprises of detected low energy photons that underwent inelastic scattering. The signal comprises of high-energy photons that underwent NRF. Thus, the current mode has significantly better signal-to-noise ratios.

4.6 Conclusion: a path forward

In this work we have presented an engineering design. This design can be used to detect or assay nuclear materials. More important than the design it is the approach described. This approach can be used for further designs with different gamma-ray sources, different materials, and different applications.

First and foremost, we endeavored to move away from a single photon counting approach. Both sources discussed in this work (HIγS and T-Rex) were exhibiting pile-up and dead time difficulties to spectral measurements. Any future source will have even higher flux and/or narrower bandwidth. Why make all those gammas just to throw most of them away because detectors can't process the signal fast enough? The approach proposed turns to the current mode of photon detection. This method scales up to any conceivable flux (as long as light-collecting

diodes on the scintillators are not saturated). We demonstrated the viability of this approach for the current source. We claim scalability of the detection approach to higher fluxes.

Second, the method analyzed here improves directly with the improvement in bandwidth of the source. The fraction of NRF-capable photons directly determines the strength of the signal. This fraction correlates with the width of NRF to bandwidth of the source ratio. Thus, free from single photon counting restrictions, integration times scale down with improvement in bandwidth.

Further experiments will prove extremely useful because measures of angular dependencies could be further refined and verified. Direct current-mode photon detection viability demonstrations might become feasible with further development of Compton sources.

Chapter 5: References

1. B. A. Ludewigt, B. J. Quiter, and S. D. Ambers. “Nuclear Resonance Fluorescence for Safeguards Applications” (LBNL Report Number LBNL-4350E) (2011).
2. Micah S. Johnson and Dennis P. McNabb. “Nuclear Resonance Fluorescence and Isotopic Mapping of Containers.” AIP Conference Proceedings 1099, 697 (2009).
3. Franz R. Metzger. “Resonance Fluorescence in Nuclei.” Prog. Nuclear Phys., Vol. 7 (1959), pp. 53–88.
4. J. D. Jackson. “Classical Electrodynamics” (3rd ed.), pp. 665–668.
5. F. V. Hartemann, F. Albert, S. S. Q. Wu, and C. P. J. Barty. “Compton scattering gamma-ray source optimization.” Presentation at 54th Annual Meeting of the APS Division of Plasma Physics.
6. D. J. Gibson, F. Albert, S. G. Anderson, S. M. Betts, M. J. Messerly, H. H. Phan, V. A. Semenov, M. Y. Shverdin, A. M. Tremaine, F. V. Hartemann, C. W. Siders, D. P. McNabb, and C. P. J. Barty. “Design and operation of a tunable MeV-level Compton-scattering-based γ-ray source.” Phys. Rev. ST -Accel. Beams 13, 070703 (2010).
7. F. Albert, S. G. Anderson, D. J. Gibson, C. A. Hagmann, M. S. Johnson, M. Messerly, V. Semenov, M. Y. Shverdin, B. Rusnak, A. M. Tremaine, F. V. Hartemann, C. W. Siders, D. P. McNabb, and C. P. J. Barty. “Characterization and applications of a tunable, laser-based, MeV-class Compton-scattering γ-ray source.” Phys. Rev. ST Accel. Beams 13, 070704 (2010).
8. D. J. Gibson, et al. “Novel Multiple-Gigahertz Electron Beams for Advanced X-Ray and Gamma-Ray Light Sources.” LDRD proposal, LNLL, page 304 of LLNL Annual Report 2012, https://st.llnl.gov/content/assets/docs/LLNL_12LDRD.pdf .
9. http://www.fel.duke.edu/lightsources/HIγS_source.pdf.
10. http://www.tunl.duke.edu/documents/public/HIGSBeamParameters.pdf.
11. Krane, Kenneth S. *Introductory Nuclear Physics,* pp. 424–431.
12. N. Petralla, et al. “Parity measurements of Nuclear Levels Using a Free Electron Laser Generated γ-Ray Beam.” PRL.88.012502 (2001).
13. J. H. Hubbell, et al. “Atomic Form Factors, Incoherent Scattering Functions, and Photon Scattering Cross Sections.” J. of Phys. Chem. Ref. Data. 4. 471 (1975).
14. J. E. Fernandez, et al. “Polarization effects on multiple scattering gamma transport.” J. of Radiation Physics and Chemistry, Volume 41, Issues 4–5, April–May 1993, pp. 579–630.
15. NIST XCOM project: http://physics.nist.gov/PhysRefData/Xcom/html/xcom1.html.
16. B. J. Quiter, et al. “Transmission Nuclear Resonance Fluorescence Measurements of 238U in Thick Targets.” Nuclear Instruments and Methods in Physics Research Section B: Beam Interactions with Materials and Atoms, Volume 269, Issue 10, 15 May 2011, pp. 1130–1139.
17. http://www.iso.org/iso/catalogue_detail?csnumber=7472.
18. http://radware.phy.ornl.gov/gf3/gf3.html#1.
19. http://www.tunl.duke.edu/Local/proposal/HIGS/pdf/Section3.pdf.

20. “Magnetic- and Electric-Dipole Excitations of 206Pb from 5.0 to 9.0 MeV,” C. W. Arnold, G. Rusev, R. Raut, J. H. Kelley, A. P. Tonchev, W. Tornow, S. L. Hammond, C. R. Howell, TUNL LPROGRESS REPORT, 1 SEPTEMBER 2011 – 31 AUGUST 2012, Triangle Universities Nuclear Laboratory, p.106
21. “Study of the Spin-Flip M1 Resonance in 206Pb,” C. Bhatia, C. W. Arnold, G. Rusev, R. Raut, J. H. Kelley, A. P. Tonchev, W. Tornow, S. L. Hammond, C. R. Howell, TUNL LI PROGRESS REPORT, 1 SEPTEMBER 2011 – 31 AUGUST 2012, Triangle Universities Nuclear Laboratory, p.101.
22. http://www.isoflex.com/isotopes/contact.html/.
23. G. Knoll, “Radiation Detection and Measurement,” 3rd edition, page 115.